HEAT TRANSFER
Edited By: William M. Worek
Online ISSN:2688-4542
Accepted August 4th 2021

Computation of unsteady Generalized Couette flow and heat transfer in immiscible dusty and non-dusty fluids with viscous heating and wall suction effects using Modified cubic B-spine Differential Quadrature Method

Rajesh Kumar Chandrawat [A], Varun Joshi[A] and O. Anwar Bég[B], Dharmendra Tripathi[#C]

[A] Department of Mathematics, Lovely Professional University Jalandhar, ***India.***
[B] Professor and Director-Multiphysical Engineering Sciences Group (MPESG), Dept. Mechanical/Aeronautical Engineering, School of Science, Engineering, Environment (SEE), Salford University, Manchester, M54WT, ***UK.***
[C] Department of Mathematics, National Institute of Technology, Uttarakhand, ***India***
Emails: rajesh.16786@lpu.co.in, varunjoshi20@yahoo.com, O.A.Beg@salford.ac.uk, [#]dtripathi@nituk.ac.in (Corresponding Author)

Abstract

In this paper, the unsteady flow of two immiscible fluids with heat transfer is studied numerically with a modified cubic B-spine Differential Quadrature Method. Generalized Couette flow of two immiscible dusty (fluid-particle suspension) and pure (Newtonian) fluids are considered through rigid horizontal channels *for three separate scenarios*: first for *non-porous plates with heat transfer*, second for *porous plates with uniform suction and injection and heat transfer*, and third for *non-porous plates with interface evolution*. The stable liquid-liquid interface is considered for the two immiscible fluids in the first two cases. In the third case, it is assumed that the interface travels from one position to another and may undergo serious deformation; hence the single momentum equation based on the (volume of fluid) VOF method is combined with the continuum surface approach model, and an interface tracking is proposed. The flow cases are considered to be subjected to three different pressure gradients, of relevance to energy systems- namely, *applied constant, decaying, and periodic pressure gradients*. For each case, the coupled partial differential equations are formulated and solved numerically using MCB-DQM to compute the fluids velocities, fluid temperatures, interface evolution. The effects of emerging thermo-fluid parameters, i. e. Eckert (dissipation), Reynolds, Prandtl, and Froude numbers, particle concentration parameter, volume fraction parameter, pressure gradient, time, and the ratio of

viscosities, densities, thermal conductivities, and specific heats on velocity and temperature characteristics are illustrated through graphs.

Keywords: *Immiscible fluids; interface tracking; modified cubic B-spline; differential quadrature method; viscous heating; energy duct transport phenomena*.

Nomenclature

$\emptyset$	Volume fraction function	g	The gravitational acceleration m/s^2
U	The velocity of the fluid m/s	l_1	The height of the interface at any point *m*
U_p	Particle phase velocity *m/s*	y_m	The average depth of the interface *m*
ρ	The density co-efficient of fluid Kg/m^3	A_0	The amplitude *m*
p	Fluid pressure *P*	K^*	Stokes drag coefficient
μ	The viscosity coefficient of fluid $kg \cdot m^{-1} \cdot$	N	the number density of the dust particles m^{-3}
ρ_p	Particle density Kg/m^3	r	The average radius of particles kg
M	The volume transfer coefficient	C_f	The Skin friction coefficient
c	The specific heat capacity of fluid $Jkg^{-1}K^{-1}$	ω	The mean free surface curvature
κ	The thermal conductivity of the fluid	σ	The interfacial tension between two liquid
c_p	specific heat capacity of the particles	R	Particle concentration parameter
T	The temperature of fluid *K*	S_1, S_2	The suction parameters
T_p	Particle phase temperature *K*	w	oscillating parameter
γ_T	temperature relaxation parameter	λ	Decaying parameter
ρ_1, ρ_2	The density co-efficient of dusty and pure	C_s	The local value of fluids concentration
m_p	The average mass of particles kg	Re	Reynolds number
μ_1, μ_2	viscosity co-efficient of dusty and pure fluids	Ec	Eckert number
κ_1, κ_2	thermal conductivities of co-efficient $\underline{W/mK}$	pr	Prandtl number
c_1, c_2	specific heat capacities of co-efficient	N_u	The Nusselt number
U_1, U_2	velocities of dusty and pure fluids m/s	Ca	Capillary number
T_1, T_2	Temperatures of dusty and pure fluids K	Fr	Froude number
t_2, t_1	temperatures of lower and upper plates K	r_1	Ratio of viscosities
C_i	Interface track	r_2	Ratio of densities
U_0	the velocity of the upper plate m/s	r_3	Particle and fluid density ratio
L_∞	The length of the upper and lower plates	C_r	The ratio of specific heat capacities
U^*	The mean flow velocity field in the channel	k_r	The ratio of thermal conductivities
ρ^*	The average density of the flow in the channel	C_{r_r}	Particle and fluid specific heat capacities ratio
μ^*	average viscosity of flow in the channel $kg \cdot$	$Ge(t)$	Time-dependent pressure gradient
F	The body force per unit mass		

1. Introduction

In many industrial problems, like splitting of the matter mostly from a fluid, oil and gas industry, petroleum filtration, polymer technology, transportation procedures, sometimes it

is hardly accessible the pure form of fluid. Similarly, some fluids include impurities such as dust particles and external entities and these types of fluids are known as dusty. *Dusty* flows or *fluid-particle suspension* dynamics have been of interest to engineers for many decades. These flows generally feature a homogenous liquid (velocity phase) carrying small dust particles (solid phase) and are also an example of a two-phase system. They arise in aerodynamics [1], chemical engineering fluidized beds [2], spinning bioreactors [3], liquid metal processing [4], nozzle systems in propulsion [5], cosmical hydrodynamics [6], and solid oxide fuel cells (SOFCs) [7]. Early work on modeling dusty fluids for the Newtonian case was reported by Saffman [8] who proposed a dusty fluid framework taking into consideration the impact of suspended particles on laminar flow stability. Marble [9] later generalized Saffman's analysis and provided a broader perspective of dusty flows deriving boundary value problems in which the dusty particles (of small volume fraction) do not interact with the momentum, heat, and/or mass transfer in such media. Marble's approach [9] also popularized the use of momentum inverse Stokes number, particle loading parameter, and temperature inverse Stokes number, which have become the basis for many subsequent dimensionless mathematical flow models. Dusty flows have also been explored in atmospheric fluid mechanics, notably foggy suspensions [10] and debris-laden tornados (swirling cone models) [11]. A number of boundary layers and fully developed flow configurations have also studied dusty (fluid-particle) suspension flows. Allaham and Peddieson [12] used a finite difference technique to compute the fluid (Newtonian) and particle-phase velocity components in swirling Von Karman flow, noting that both the particle phase viscosity and solid surface boundary conditions impact considerably on the dynamics. Manuilovich [13] investigated the transient flow of a dilute gas-particle dusty mixture in a plane channel under the action of a constant longitudinal pressure gradient and transverse gravity force, with asymptotic and numerical methods for the cases of both monodisperse and polydisperse particles. Bilal *et al.* [14] studied the viscoelastic dusty fluid-free convective hydromagnetic Couette flow in a rotating frame using a Poincare-Light Hill Technique. They computed the particle and fluid phase velocities and also derived expressions for skin friction and Nusselt number (the rate of heat transfer) are also calculated. It was observed that stronger rotation decelerates both dust particle phase and fluid phase velocities. Osiptsov [15] used Van Dyke's matched asymptotic expansion method to compute the dusty laminar boundary layer flow from both plane and curved surfaces, scrutinizing the impact of particle accumulation in the boundary layers and the effects of particles on the friction and heat fluxes. Oscillatory

hydromagnetic channel flow of dusty fluids was considered by Debnath and Ghosh [16]. Dey [17] analyzed the non-Newtonian dusty channel convective flow problem with viscous heating effects. Pulsatile time-dependent dusty pumping in a channel was examined by Datta *et al.* [18] using Laplace transform techniques. Vajravelu *et al*. [18] studied temperature-dependent fluid property effects in magnetized convective boundary layer flow in a dusty fluid over a stretching sheet with the second-order implicit finite difference scheme known as the Keller–Box method and perturbation methods. They observed that transverse fluid phase velocity is damped with elevation in the fluid-particle interaction parameter both with and without magnetic field. Kumar and Sarma [20] used the least-squares finite element method to simulate the steady flow of a fluid-particle suspension generated by stretching a wall, noting that both fluid and particle-phase velocities are suppressed with increment in particle loading and fluid-particle interaction parameters. They also observed that dusty particle density attains a peak at the plate (sheet) surface. Dalal *et al.* [21] presented central and second upwind finite difference computational solutions for natural convection of a dusty fluid in an infinite rectangular channel with differentially heated vertical walls and adiabatic horizontal walls. They noted that the heat transfer rate at the channel walls (Nusselt number) is reduced with an increase of mass concentration of dust particles, whereas it is boosted with a higher thermal buoyancy effect (Rayleigh number). Gretler and Regenfelder [22] developed similarity solutions for adiabatic strong blast shock waves of variable energy propagating in a dusty gas using an equilibrium-flow condition and simulating the variable energy input via a driving piston (decelerated, constant velocity, or accelerated) with a time-dependent power law. They tabulated extensive results for the effects of mass concentration of the solid particles and the ratio of the density of solid particles to the constant initial density of the gas. Saqib *et al.* [23] used a two-phase Brinkman model with Laplace and Hankel transforms to develop exact analytical solutions for magnetic blood flow in a cylindrical tube with Newtonian fluid and uniformly distributed magnetite dusty particles. Park and Rosner [24] computed laminar flow mass, momentum, and energy-transfer rate coefficients over a wide range of particle mass loadings, dimensionless particle relaxation times (Stokes numbers), dimensionless thermophoretic diffusivities, and gas Reynolds numbers in steady axisymmetric “dusty-gas” flow between two infinite disks. They identified a new “critical” Strokes number (for incipient particle impaction) on the particle mass loading and the wall/gas temperature ratio for dust-laden gas motion towards “overheated” solid surfaces. Takhar *et al.* [25] deployed a complex variable method to study the

transient magnetic flow of a dusty viscous liquid in a spinning channel with Hall current effects, elucidating in detail the impact of Strouhal and Stokes numbers on particle and fluid phase velocities at both weak and strong magnetic fields. Chakma [26] derived closed-form solutions for dual-phase velocities, displacement thicknesses, and skin friction for dusty Newtonian flow in a channel with perforated walls considering both suction and injection (blowing) effects. Bég *et al*. [27] used a variational finite element method to compute the steady, laminar nonlinear natural convection dusty flow with heat generation in a vertical channel containing a non-Darcian porous medium. They computed both fluid/particle-phase velocity and temperatures, noting that fluid velocity is strongly damped with porous drag forces and magnetic field whereas particle-phase velocity is weakly reduced. They further noted that higher inverse momentum Stokes number suppresses fluid phase velocity but elevates particle-phase velocity. Further recent studies of dusty transport in channels have been reported by S. Mukhopadhyay *et al.* [28] (using a finite volume method for a wavy-walled duct), Bég *et al.* [29] (using differential transform methods with Padé approximants for dusty blood flow under thermal buoyancy effects) and Palani *et al.* [29] (with a Crank–Nicholson finite difference method for external cylinder coating dusty boundary layer).

Many flow configurations arising in industrial materials processing, nuclear engineering, and petrochemical systems feature two-fluid flows. These relate to the presence of two viscous liquids which do not mix i. e. are *immiscible*. Comprehensive discussions on such flows have been given by Corey [31] and Briscoe *et al.* [32] for geological and chemical engineering colloidal applications, respectively. As noted, immiscible or stratified flows are also critical in nuclear engineering, specifically in the late in-vessel stage of core melt severe accidents of a nuclear reactor [33]. These flows are also relevant to liquid polymer layers on a solid substrate [34]. Many theoretical and numerical studies of two-fluid flow transport phenomena have therefore been communicated. Nikodijević *et al.* [35] studied theoretically the thermal convection of electrically conducting immiscible Newtonian fluids in channel flow under an oblique magnetic field. Mori *et al*. [36] used a moving finite element method to compute the transient two-phase free sharp interface problem arising in the flow of two immiscible fluids (slag and molten metal) in a blast furnace with an implicit time-stepping scheme. Tang and Wrobell [37] employed a volume-of-fluid (VOF) method interface tracking method for modeling the flow of immiscible metallic liquids in mixing processes, noting that the mixing of immiscible metallic liquids is greatly impacted by the viscosity of the system, shear forces, and turbulence. Wan *et al*. [38] deployed an implicit

hybrid finite element/volume (FE/FV) solver to flows involving two immiscible fluids, using a segregated pressure correction or projection method on staggered unstructured hybrid meshes. They captured the fluid interface by solving an advection equation for the volume fraction of one of the fluids which achieve an improved interface sharpening strategy by reducing the smearing of the interface over time. Than *et al.* [39] investigated the hydrodynamic stability of plane Poiseuille flow of two immiscible liquids of different viscosities and equal densities, noting the sensitivity of results to the viscosity and volume ratio. They identified that high viscosity fluid centrally located achieves good stability whereas centrally located layers of less viscous fluid (fingering zones) are consistently unstable. Yagodnitsyna *et al.* [40] simulated the flow patterns of immiscible liquid-liquid flow in a rectangular microchannel with T-junction for three liquid-liquid flow systems (kerosene – water, paraffin oil-water, and castor oil – paraffin oil), and included a variety of analyses for parallel flow, slug flow, plug flow, dispersed (droplet) flow, and rivulet flow at different velocity ratios for different Weber and Ohnesorge numbers. Bég *et al.* [41] analyzed the unsteady hydromagnetic flow of two immiscible Newtonian fluids in a rigid horizontal channel containing two non-Darcian porous media with oscillating lateral wall mass flux under a sinusoidal pressure gradient. They deployed forward time/central space (FT/CS) finite-difference and Galerkin finite-element methods, observing a strong modification in velocity components with inertial and magnetic field effects. Zhou *et al.* [40] implemented a meshless Local Petrov–Galerkin method with Rankine source solution (MLPG_R method) to compute two-fluid Newtonian flows with both low density and very high density-ratios. Further investigations include McLean *et al.* [41] and Bittlseton *et al.* [42] (on primary cement displacement immiscible flows in oil well systems) and Tang *et al.* [43] (on 2- and 3-dimensional piecewise linear (PLIC) volume-of-fluid (VOF) Eulerian grid computation of immiscible twin-screw extruder interfacial flows). Borrelli *et al.* [46] considered two immiscible Newtonian fluids in a vertical channel and studied the magneto-convection parameter effects on flow behavior. In many of these studies, a significant challenge has been the correct analysis of the complex interface between the immiscible liquids. The interface travels from one position to another and can also be considerably deformed or in extreme cases may collapse. Hence the interface between two immiscible fluids plays a vital role in computational flow simulation, and it should be determined as one major component of the solution. The nonlinear behavior of a sheared immiscible fluid interface is studied by Tauber *et al.* [47]. Umavathi and Bég [48] deployed a finite difference code and special interfacial stress

conditions to compute the influence of thermal conductivity ratio and viscosity ratio on interfacial heat and momentum transfer for two Newtonian immiscible fluids in a vertical duct with non-isothermal wall conditions. They showed that with different duct aspect ratios in the upper and lower duct regions a marked movement of the interface is generated. Yih [49] observed that owing to the viscosity drop from one fluid to another, the tangential velocity gradient also shifts and this contributes to instability in the interface. Dong [50] used a Lattice Boltzmann code to simulate immiscible fluids displacement. There are several techniques of interface monitoring, such as the front tracking, moving grid, the level set, and volume of fluid (VOF) technique. This approach offers a clear and straightforward way of addressing geometrical changes in the interface. DeBar [51] pioneered the VOF method, developing the first comprehensive numerical code for Eulerian hydrodynamics in the compressible non-viscous flow of several fluids in two-dimensional (axially symmetric) regions. Youngs [52] did some significant modifications to this code by incorporating viscous and large interface deformation features. Li and Renardy [53] studied the interface between two immiscible fluids by the VOF method. The tracking of the interface between two immiscible fluids was explored via various methods, including VOF by Gopala and Wachem [54].

The investigation of a dielectric viscous fluid flowing via channels under the presence of an external magnetic field is not only intriguing conceptually, but it also has implications in the mathematical modeling of a variety of industrial and biological systems. The homotopy perturbation technique is applied to find the solutions to the system of modeled differential equations for Williamson nanofluid flow with external magnetic effect Bhatti *et.al* [55]. The MHD effect on micropolar nanofluid is studied by Hsiao [56]. The blood flow with floating magnetic Zinc-oxide nanoparticles in the arteries is analyzed by Zhang *et.al* [57]. The effects of applied magnetic field on hybrid bio-nanofluid flow in a peristaltic duct are investigated by Bhatti *et.al* [58] Hsiao [59] investigated an electrical MHD ohmic dissipation energy release on Carreau-Nanofluid. Bibi *et.al* [60] [61]did the numerical analysis of magnetohydrodynamics effect on Williamson and tangent hyperbolic fluid. Some more studies on MHD flow can be seen in [62]–[64]

Another key aspect of interfacial two-fluid dynamics is the effect of time. Despite its essential importance, relatively little work has been conducted regarding the time-dependent unstable flow of two immiscible liquids. The unsteady multiphase flow problem has been explored however via

the front tracking method by Tryggvason *et al.* [65]. Riaz *et al.* [66] studied the instability of immiscible two-phase flow in porous media. In addition to VOF methods, other numerical algorithms have also been deployed in interfacial flows. These include spectral, alternating direction implicit (ADI) finite difference, finite element, and meshless smoothed particle hydrodynamics (SPH). Devakar and Raje [67] numerically explored the time-dependent unsteady flow of two immiscible fluids by the Crank-Nicolson finite difference method. The low-order approaches do use several grid points to achieve an acceptable degree of accuracy to obtain specific outcomes at such defined points. The differential quadrature method (DQM) approach was proposed by Bellman[68] developed an improved discretization strategy to produce concise numerical solutions with significantly reduced grid sizes. DQM was further improved by Quan and Chang [69], [70] motivated by chemical engineering applications. Various test functions, namely, Lagrange interpolation polynomials, sink and spline, cubic and modified cubic B-spline functions, have also been explored in many articles - see [71]- [77] - for the calculation of weighting coefficients in DQM. This technique is also convenient to use and financially efficient with data complexity, leading to error mitigation and easy implementation. Using the DQM, Katta and Joshi [78] analyzed the behavior of elastico-viscous magneto-hydrodynamic fluid in a parallel plate channel. Katta *et al.* [79] numerically explored the unsteady fluid flow of two immiscible fluids with the DQM approach.

To the best knowledge of the authors, no attempt has been made to study the *unsteady flow of two immiscible dusty and non-dusty fluids with heat transfer and interface evolution.* This flow regime has important applications in nuclear reactor designs and also thermal duct systems in petrochemical engineering. The computational approach adopted in this paper is a modified cubic B-spine Differential Quadrature Method. Generalized Couette flow of two immiscible dusty (fluid-particle suspension) and pure (Newtonian) fluids are considered through rigid horizontal channels *for three separate schemes*: first for *non-porous plates with heat transfer*, second for *porous plates with uniform suction and injection and heat transfer*, and third for *non-porous plates with interface evolution*. A detailed appraisal of the physics is included. Validation is also conducted through skin friction coefficient and Nusselt number. The advection and reconstruction/tracking of the interface for the third scheme is also explored. MCB-DQM is shown to achieve exceptional stability and accuracy and offers significant promise in simulating interfacial duct flows in nuclear and geothermal energy, petrochemical transport, and materials processing systems. Three different

pressure gradients are studied, viz *applied constant, decaying, and periodic pressure gradients*. The fluid and particle velocities, temperatures, and also interface tracking are computed by solving coupled partial differential equations. Detailed graphical visualizations are included and a comprehensive elaboration of the physical implications provided.

2. Transport model formulation for dusty-Newtonian immiscible flows

Motivated by nuclear engineering applications, in this study, incompressible, immiscible two-fluid dusty-Newtonian channel convective heat transfer flows are considered for a variety of boundary conditions. It is important to note that as the particles are non-interacting, all dusty particles in a local volume have the same velocity vector and temperature (ballistic collisions and Brownian dynamics are ignored, following Marble [10]). The formulation adopted for the field equations governing the fluid and particulate phases following Ramesh *et al*. [80], Abdulsalam *et al.* [81], and Attia *et al.* [82] and takes the form:

$$\frac{\partial \emptyset}{\partial t} + \nabla.((1-\emptyset)U) = 0 \tag{1}$$

$$\frac{\partial \emptyset}{\partial t} + \nabla.(\emptyset U_p) = 0 \tag{2}$$

$$\rho(1-\emptyset).\left(\frac{\partial U}{\partial t} + U.\nabla\, U\right) = (1-\emptyset)(-\nabla p + \mu\nabla^2 U) - M\rho_P\emptyset(U-U_p) \tag{3}$$

$$\rho_p\emptyset\,\left(\frac{\partial U_p}{\partial t} + U_p.\nabla U_p\right) = M\rho_p\emptyset\left(U-U_p\right) \tag{4}$$

$$\rho c(1-\emptyset).\left(\frac{\partial T}{\partial t} + U.\nabla T\right) = (1-\emptyset)\kappa\nabla^2 T - (1-\emptyset)\mu(\nabla U)^2 - \rho_p c_p\frac{\emptyset(T-T_p)}{\gamma_T} + M\rho_p\emptyset\left(U-U_p\right)^2 \tag{5}$$

$$\rho_p c_p\emptyset\,\left(\frac{\partial T_p}{\partial t} + U_p.\nabla T_p\right) = -\rho_p c_p\frac{\emptyset(T_p-T)}{\gamma_T} \tag{6}$$

Here $\emptyset$ is the particle volume fraction, U is the velocity of the fluid. U_p is the velocity of a dust particle, ρ is the density co-efficient of fluid, p is the fluid pressure at any point, ρ_p is the density of dust particles, the material constants μ is viscosity coefficients, and M is the volume transfer coefficient. At constant volume, c is the specific heat capacity of fluid, κ is the thermal conductivity of fluid, c_p is the specific heat capacity of the dust particle. Heat transfer takes place via thermal conduction through the fluid from the top hot plate to the bottom cold plate. Dust particles receive temperature from the conduction through their rounded texture. T is the

temperature of fluid and T_p is the temperature of dust particles and γ_T is the temperature relaxation time. Some assumptions have been made to develop the governing equations regarding the analysis of dusty fluids (fluid-particle suspension). The fluid is incompressible, and the density is believed to be stable for both phases. The dust particles are in an electro-free form and circular in shape. All the dust particles have the same size, mass, and un-deformable constitution and are evenly distributed throughout the fluid. If the dusty fluid flows across the porous plates, then particles do not penetrate the boundaries. It is also implicit that the particle phase is sufficiently dilute so that the interactions between any two particles are ignored, and the dust particle size is also relatively tiny in scale. Hence the net dust effect on the fluid particles is equivalent to the additional force, $M\rho_p\emptyset(U - U_p)$ per unit volume. One can see that, in the absence of dust particles in the fluid $\left(U = U_p, T_p = T \right)$ the velocity and temperature distribution

equations (3) and (5) reduces to:

$$\rho(1-\emptyset).\left(\frac{\partial U}{\partial t} + U.\nabla\, U\right) = (1-\emptyset)(-\nabla p + \mu\nabla^2 U) \quad (7)$$

$$\rho c(1-\emptyset).\left(\frac{\partial T}{\partial t} + U.\nabla T\right) = (1-\emptyset)\kappa\nabla^2 T - (1-\emptyset)\mu(\nabla U)^2 \quad (8)$$

2.1. The volume of the fluid (VOF) model

In the system of two immiscible liquids, the characteristics described by the momentum model are defined by the existence of each control volume. The average density and viscosity quantities are normalized by the following equations Li and Renardy [83]:

$$\rho^* = \rho_1 + C_s(\rho_2 - \rho_1) \quad (9)$$

$$\mu^* = \mu_1 + C_s(\mu_2 - \mu_1) \quad (10)$$

Where ρ_1, μ_1 be the density and viscosity of the non-dusty (pure)fluid and ρ_2, μ_2 be the density and viscosity of the dusty fluid? The concentration parameter C_i is used to track the interface and transported by the mean velocity field U^*.

$$\frac{\partial C_i}{\partial t} + U^*.\nabla C_i \ = 0 \quad (11)$$

The incompressible flow velocity is driven by a single momentum equation, with the resultant velocity field shared between the transitions Li and Renardy [83]:

$$\rho^*(\frac{\partial U^*}{\partial t} + U^*.\nabla U^*) = -\nabla p + \mu^*\nabla^2 U^* + F \quad (12)$$

Here the body forces *F* is included with gravitational force and interfacial tension and$-\nabla p$ is the applied pressure term.

2.2. Formulation of dusty and pure fluid flow under the scheme – I

Consider the unsteady, fully developed, laminar, and unidirectional Generalized Couette flow of two immiscible dusty (fluid-particle suspension) and pure(non-dusty Newtonian) fluids shown in Figure 1(a). Some assumptions are being made under the scheme-I. Both fluids are immiscible, viscous, and incompressible, and move between two horizontal parallel non-porous plates (two-dimensional channel). Both plates are electrically non-conductive with zero polarization voltage. The plates are in opposition to each other and occupy the *x*-*z* plane as depicted in Figure 1 (a). The lower plate is stationary and has a steady temperature of t_1, while the upper plate travels at a fixed velocity of U_0 in the *x*-(axial) direction at a constant temperature of t_2. Here $t_2 > t_1$. Pure Newtonian fluid occupies the bottom region -I($-k \leq y \leq 0$) and has a fluid velocity U_1, density ρ_1, viscosity μ_1, specific heat capacity $c_1$of fluid at constant volume, temperature $T_1$and thermal conductivity κ_1.Dusty fluid occupies the upper region -II ($0 \leq y \leq k$) and has fluid velocity U_2, density ρ_2, viscosity μ_2, specific heat capacity c_2 of fluid at constant volume, temperature T_1, thermal conductivity κ_2. In the dusty fluid, the dust particles possess a particle velocity U_p, density ρ_p, specific heat capacity $c_p$of a particle at constant volume, temperature T_p and thermal conductivity κ_p. The transportation attributes are unchanged in both the regions and common pressure gradients are applied from the vertical *y*-direction. The flow of dusty fluid in the region –II is governed by the equations (1), (2), (3), and (4). In the absence of dust particles in the region I, the pure fluid flow (Newtonian i.e., non-dusty) is governed by equations (1), (7), and (8).

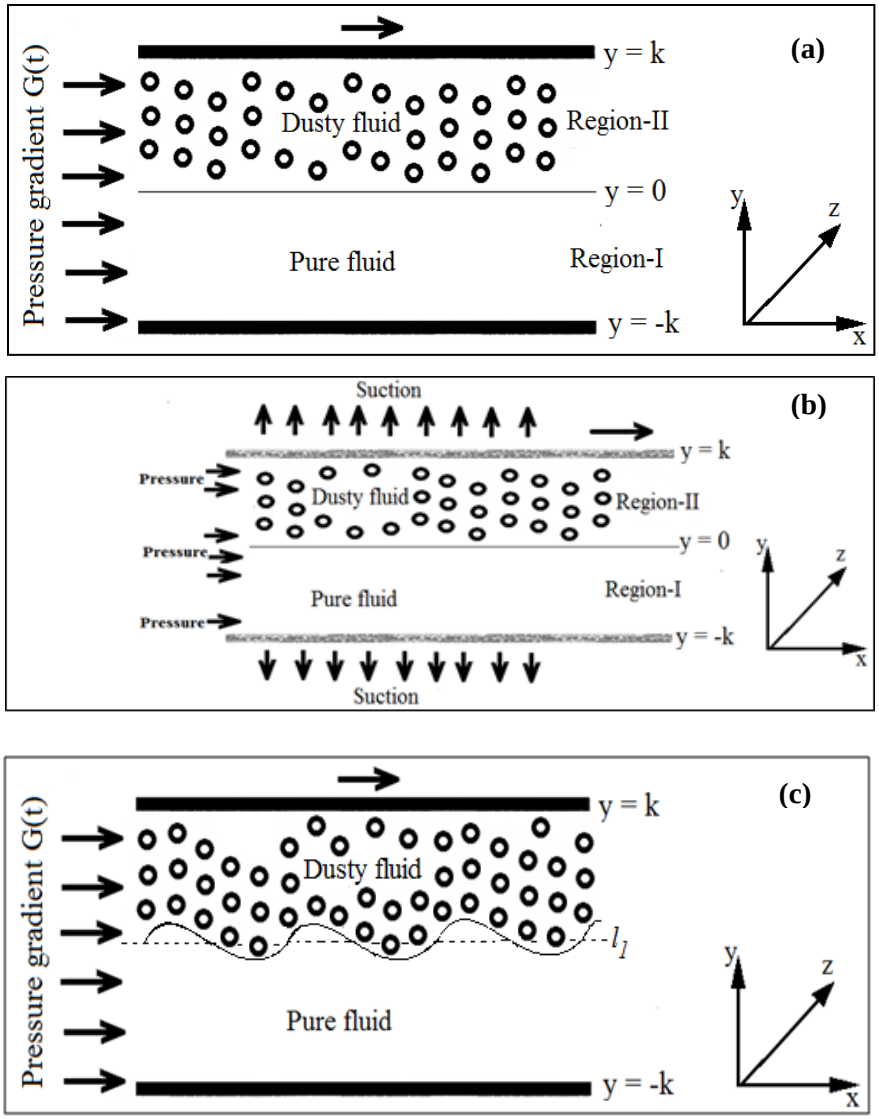

Figure 1 Geometrical configuration for Generalized Couette flow of immiscible (a) dusty and pure (Newtonian) fluids under the scheme-I, (b) scheme-II, and (c) under the scheme-III.

The fluid velocity vector ($U_i(y,t)$) and temperature ($T_i(y,t)$) are assumed to be in both regions (i=*I, II*) (U_i=($U_i(y,t)$,0,0) and (T_i=($T_i(y,t)$,0,0) and particle velocity and temperature vectors in region II are presumed as (U_p=($U_p(y,t)$,*0,0*) and (T_p=($T_p(y,t)$,0,0), respectively. The hydrodynamic motion is driven by an applied pressure gradient in the *x*-axial direction; therefore, the velocity profile is unidirectional. Thus, $\nabla U_i = U_{i_y}, \nabla^2 U_i = U_{i_{yy}}$, $\nabla T_i = T_{i_y}, \nabla^2 T_i = T_{i_{yy}}$. The fluid layers are mechanically coupled through the model of momentum exchange. Transferring momentum arises through consistency in velocity and shear stress over the interface. However, we assume that the flow rate and shear-induced pressure are also stable at the interface between two

liquids. Fluid flow and temperature distribution, in view of the above constraints, are governed by the following equations:

Region-I *(Pure fluid: $-k \le y \le 0$).*

$$\rho_1 . \frac{\partial U_1}{\partial t} = -\nabla P + \mu_1 \nabla^2 U_1 \quad (13)$$

$$\rho_1 c_1 . \frac{\partial T_1}{\partial t} = \kappa_1 \nabla^2 T_1 - \mu_1 (\nabla U_1)^2 \quad (14)$$

Region-II *(Dusty fluid: $0 \le y \le k$)*

$$\rho_2 . \frac{\partial U_2}{\partial t} = -\nabla P + \mu_2 \nabla^2 U_2 - M \rho_p \emptyset \frac{(U_2 - U_p)}{(1-\emptyset)} \quad (15)$$

$$\frac{\partial U_p}{\partial t} = M(U_2 - U_p) \quad (16)$$

$$\rho_2 c_2 . \frac{\partial T_2}{\partial t} = \kappa_2 \nabla^2 T_2 - \mu_2 (\nabla U_2)^2 - \frac{\rho_p c_p \emptyset (T_2 - T_p)}{\gamma_T (1-\emptyset)} + M \rho_p \emptyset \frac{(U_2 - U_p)^2}{(1-\emptyset)} \quad (17)$$

$$\frac{\partial T_p}{\partial t} = -\frac{(T_p - T_2)}{\gamma_T} \quad (18)$$

Classical hyper-stick and no-slip boundary conditions are considered and can be numerically prescribed:

Initial conditions: At $t \le 0$, $U_1(y,t) = T_1(y,t) = 0, for -k \le y \le 0$,

$$U_2(y,t) = U_p(y,t) = 0 \; and \; T_2(y,t) = T_p(y,t) = 0 \; for \; 0 \le y \le k \quad (19)$$

Boundary and interface conditions: At $t > 0$,

$$U_1(-k,t) = 0, U_2(k,t) = U_p(k,t) = U_0, T_1(-k,t) = t_1, T_2(k,t) = T_p(k,t) = t_2 ,$$

$$U_1(0,t) = U_2(0,t), T_1(0,t) = T_2(0,t), and \; at \; y = 0, \; \mu_1 U_{1_y} = \mu_2 U_{2_y} , \kappa_1 T_{1_y} = \kappa_2 T_{2_y}. \quad (20)$$

Introducing the non-dimensional parameters: $\bar{x} = \frac{x}{k}, \bar{y} = \frac{y}{k}, , \overline{U_1} = \frac{U_1}{U_0}, \overline{U_2} = \frac{U_2}{U_0}, \overline{U_p} = \frac{U_p}{U_0}$,

$$\bar{p} = \frac{p}{\rho_1 {U_0}^2}, \bar{t} = \frac{t U_0}{k} , \overline{T_1} = \frac{T_1 - t_1}{t_2 - t_1} , \overline{T_2} = \frac{T_2 - t_2}{t_2 - t_1}, \overline{T_p} = \frac{T_p - t_2}{t_2 - t_1} \quad (21)$$

Where $M = \frac{6\pi r \mu_2}{m_p}$ is the volume transfer coefficient with an average mass of dust particle m_p and radius r. Hence the last term of equation (16) $M \rho_p \emptyset \frac{(U_2 - U_p)}{(1-\emptyset)}$ can be written as $\frac{R * r_1}{Re * r_2}(U_2 - U_p)$. Here $R = \frac{K^* N k^2 \emptyset}{\mu_2 (1-\emptyset)}$ is particle concentration parameter and $K^* = 6\pi r \mu_2 U_0$ is the Stokes drag coefficient, N is the number density of particle per unit volume, and $Re = \frac{\rho_1 U_0}{\mu_1}$ is the Reynolds

number. $r_2 = \frac{\mu_2}{\mu_1}, r_1 = \frac{\rho_2}{\rho_1}$ are the viscosity and density ratios for the two immiscible fluids in zones I and II, respectively. Hence the last term of equation (17) is updated accordingly where $r_3 = \frac{\rho_2}{\rho_p}$ is the ratio of the density of fluid and dust particles in region II. In equation (17) and (18) $\gamma_T = \frac{3}{2}\frac{\rho_p.c_p.\mu_2}{K^*.N.\kappa_2}$ *i*s the temperature relaxation time where the Prandtl number (ratio of momentum and thermal diffusivity) is $pr = \frac{c_1 * \mu_1}{\kappa_1}$. $Ec = \frac{U_0}{c_1(t_2 - t_1)}$ is the Eckert number which is the ratio of the kinetic energy of the flow to the enthalpy difference (viscous dissipation). $k_r = \frac{\kappa_2}{\kappa_1}$ is the ratio of thermal conductivity. $C_r = \frac{c_2}{c_1}$ is the ratio of specific heat. $C_{r_r} = \frac{c_2}{c_p}$ is the ratio of specific heat of fluid and dust particle in region II. $-\nabla p = -\partial p/\partial x = Ge(t)$ is the applied *time-dependent* pressure gradient in the x-axial direction with $t > 0$. Three distinct cases for $Ge(t)$ are considered to analyze the numerical results:

Case-I: $Ge(t) = Ge$ (when the flow is induced by applied *constant* pressure gradient)

Case-II: $Ge(t) = Ge * Sin(wt)$ (when the flow is induced by applied *periodic* pressure gradient with oscillating parameter w)

Case-III: $Ge(t) = Ge * e^{-\lambda t}$ (when the flow is induced by a *decaying* pressure gradient with the *decaying parameter,* λ).

After dropping the bars and introducing the above non-dimensional parameters, appropriate initial, interfacial, and boundary conditions according to the scheme-I, the equation (13) can be modified as follows:

Region-I ($-k \leq y \leq 0$) (Pure Newtonian fluid region):

$$U_{1_t} = Ge(t) + \frac{U_{1yy}}{Re} \tag{22}$$

$$T_{1_t} = \frac{T_{1yy}}{Re * pr} + \frac{Ec}{Re}\left(U_{1_y}\right)^2 \tag{23}$$

Region-II (0 ≤ y ≤ k) (Dusty fluid):

$$U_{2_t} = \frac{Ge(t)}{r_1} + \frac{r_2}{r_1}\frac{U_{2yy}}{Re} - \frac{R * r_2}{r_1}\frac{(U_2 - U_p)}{Re} \tag{24}$$

$$U_{p_t} = \frac{R * r_3 * r_2}{r_1}\frac{(U_2 - U_p)}{Re} \tag{25}$$

$$T_{2_t} = \frac{\boldsymbol{k_r}*T_{2_{yy}}}{\boldsymbol{C_r}*r_1*Re*pr} + \frac{r_2}{\boldsymbol{C_r}*r_1}\frac{Ec}{Re}\left(U_{2_y}\right)^2 + \frac{2}{3}\frac{R*\boldsymbol{k_r}}{\boldsymbol{C_r}*r_1*pr}\frac{(T_p-T_2)}{Re} + \frac{R*r_3*r_2}{r_1}\frac{(U_2-U_p)^2}{Re} \quad (26)$$

$$T_{p_t} = \frac{2}{3}\frac{R*\boldsymbol{k_r}*\boldsymbol{C_{r_r}}*r_3}{\boldsymbol{C_r}*r_1*pr}\frac{(T_2-T_p)}{Re} \quad (27)$$

Initial, boundary and interfacial conditions are considered as equation (19-20) with *k=1*, $U_0 = 1$, $t_1 = 0, t_2 = 1$.

2.2.1The Nusselt number and skin friction coefficients

When the fluid flows over the plates, it exerts a frictional effect on the plates' surfaces, obstructing forward motion and causing skin friction drift on the surface. The skin-friction co-efficient is used to quantify this effect.

The expression of Nusselt *number and skin friction coefficients* at both plates are calculated as$(\boldsymbol{N_u})_{y=-1} = \left(-\boldsymbol{T_{1_y}}\right)_{y=-1}, (\boldsymbol{N_u})_{y=1} = \left(-\boldsymbol{T_{2_y}}\right)_{y=1}, (\boldsymbol{C_f})_{y=-1} = \left(\frac{\boldsymbol{2U_{1_y}}}{\boldsymbol{Re}}\right)_{y=-1}, (\boldsymbol{N_u})_{y=1} = \left(\frac{\boldsymbol{2r_2U_{2_y}}}{\boldsymbol{r_1Re}}\right)_{y=1}$ *(28)*

2.3. Formulation of dusty and pure fluid flow under the scheme-II

Consider again the unsteady, fully developed, laminar, and unidirectional Generalized Couette flow of pure and dusty fluids in a horizontal channel shown in Figure 1(b). Let $U = U_i\,(y,t)i + U_0{}^*j + U_k\,k.$ be the velocity vector of fluids. Both plates have long length, say L_∞ and $S^*{}_i (i = I, II)$ is the volume of fluid sucked per unit length of the lower and upper plate, respectively (the plates are porous and wall transpiration is possible). Hence $S^*{}_i * L_\infty$ is the total volume of fluid sucked by the respective plate, and the same amount of fluid is mechanically injected. A uniform suction from the upper and a uniform injection are applied on the dusty fluid in region II; similarly, a uniform suction from the lower and a uniform injection in the *y*-direction are applied on the pure Newtonian fluid in region I. The size, mass, and radius of dust particles, and other fluids credentials are similar to the scheme -I flow except the uniform suction and injection effect [72] $S_1 = S_2 = \frac{U_0{}^*}{U_0}$.

After dropping the bars and introducing the non-dimensional parameters, initial, interfacial, and boundary conditions according to the scheme-I flow the governing equations for fluids and particle-phase equations (3-6) in both the regions of scheme-II flow emerge as:

Region-I ($-k \le y \le 0$) (Pure fluid region):

$$U_{1_t} = Ge(t) + \frac{U_{1_{yy}}}{Re} - S_1 U_{1_y} \quad (29)$$

$$T_{1_t} = \frac{T_{1_{yy}}}{Re*pr} - S_1 T_{1_y} + \frac{Ec}{Re}\left(U_{1_y}\right)^2 \quad (30)$$

Region-II for Dusty fluid ($0 \le y \le k$):

$$U_{2_t} = \frac{Ge(t)}{r_1} + \frac{r_2}{r_1}\frac{U_{2_{yy}}}{Re} - \frac{R*r_2}{r_1}\frac{(U_2 - U_p)}{Re} - S_2 U_{2_y} \quad (31)$$

$$U_{p_t} = \frac{R*r_3*r_2}{r_1}\frac{(U_2 - U_p)}{Re} \quad (32)$$

$$T_{2_t} = \frac{\boldsymbol{k_r}*T_{2_{yy}}}{\boldsymbol{C_r}*r_1*Re*pr} - S_2 T_{2_y} + \frac{r_2}{\boldsymbol{C_r}*r_1}\frac{Ec}{Re}\left(U_{2_y}\right)^2 + \frac{2}{3}\frac{R*r_2*\boldsymbol{k_r}}{\boldsymbol{C_r}*r_1*pr}\frac{(T_p - T_2)}{Re} + \frac{R*r_3*r_2}{r_1}\frac{(U_2 - U_p)^2}{Re} \quad (33)$$

$$T_{p_t} = \frac{2}{3}\frac{R*\boldsymbol{k_r}*\boldsymbol{C_{r_r}}*r_3}{\boldsymbol{C_r}*r_1*pr}\frac{(T_2 - T_p)}{Re} \quad (34)$$

Initial, boundary and interfacial conditions are considered as equation (19-20) with $k=1$, $U_0 = 1$, $t_1 = 0, t_2 = 1$.

2.4. Formulation of interface reconstruction and averaged flow of dusty and pure fluids under the scheme-III

In this third scenario, again we study the Generalized Couette flow of two immiscible, pure, and dusty fluids undergoing shearing motions; however, we assumed that owing to a *viscosity jump*, interfacial instability occurs. All other assumptions are as in schemes I and II. Scheme III is visualized in Figure 1(c). The lower plate is stationary while the upper plate travels at a fixed velocity of U_0 in the x-axial direction. Let ρ_1, μ_1 be the density and viscosity of pure fluid which lies in the region $(-k \le y \le l_1)$ with the interface height from the lower plate, l_1. The dusty fluid has the density ρ_2 and the viscosityμ_2 occupies in $(l_1 \le y \le k)$. The *evolution of the interface* is analyzed by using horizontal attenuation in the initial interface phase. Let the initial interface be an Eigen-mode say $l_1 y_m + A_0 cos(B_0 y)$ where y_m is the average depth of interface and A_0, B_0 are the amplitude and wavenumber. The dust particles have the same size and a circular shape, mass, and un-deformable electro-free form. They are evenly spread across the fluid in the region with density ρ_p. The particle phase is sufficiently distilled so that the interactions between any two dust particles are ignored, and the dust particle size is also relatively tiny in scale but affects the mean flow velocity U^*. The flow of these immiscible fluids acquires momentum due to the common pressure gradient which is applied in the direction of the x-axis with an average density $\rho^* = \rho_1 + C_s(\rho_2 - \rho_1)$and viscosity$\mu^* = \mu_1 + C_s(\mu_2 - \mu_1)$.The flow velocity U^*, particle velocity U_p and interface track C_i vectors are presumed as U^*= $(U^*(y,t)$,0,0),(U_p=$(U_p(y,t)$,0,0)

and (C_i=($C_i(y,t)$,0,0), respectively. The movement of fluids is incompressible unsteady and is driven by an applied pressure gradient in the *x*-axial direction; therefore, the velocity profile is unidirectional. Thus,$\nabla U^* = \frac{\partial U^*}{\partial y}, \nabla^2 U^* = \frac{\partial^2 U^*}{\partial y^2}, \nabla C_i = \frac{\partial C_i}{\partial y}$, $\nabla^2 C_i = \frac{\partial^2 C_i}{\partial y^2}$. The fluid layers are mechanically coupled through the model of momentum exchange. The movement of the interface between two immiscible fluids of distinct density and viscosity is described by the local value of concentration parameter as volume fraction between two immiscible liquids C_s, and the interface is characterized by the following constraints.

$$C_s = \begin{cases} 0 & outside\ the\ s^{th}\ fluid \\ > 0, < 1 & at\ the\ s^{th}\ fluid\ interface \\ 1 & inside\ the\ s^{th}\ fluid \end{cases} \quad (35)$$

Depending on the local value of C_s the necessary attributes and variables are allocated to each control volume inside the domain. Hence by using the equations (3),(4),(11), and (12), the averaged flow is governed as ($-k \le y \le k$).

$$\frac{\partial C_i}{\partial t} + U^* \frac{\partial C_i}{\partial y} = 0 \quad (36)$$

$$\rho^* \frac{\partial U^*}{\partial t} = -\nabla P + \mu^* \frac{\partial^2 U^*}{\partial y^2} - M\rho_p (U^* - U_p) + F \quad (37)$$

$$\frac{\partial U_p}{\partial t} = M\left(U^* - U_p\right) \quad (38)$$

Again, classical hyper-stick and no-slip boundary conditions are considered. The relevant initial and boundary conditions take the form:

Initial conditions: At $t \le 0, U^*(y,t) = U_p(y,t) = 0,\ C_i(y,t) = A_0 cos(B_0 y)$ (39)

Boundary conditions: At $t > 0$,

$$U^*(-k,t) = U_p(-k,t) = 0,\ U^*(k,t) = U_p(k,t) = U_0 \quad (40)$$

Again, introducing the non-dimensional parameters: $\bar{x} = \frac{x}{k}, \bar{y} = \frac{y}{k}, \overline{U^*} = \frac{U^*}{U_0}, \overline{U_p} = \frac{U_p}{U_0}, \bar{p} = \frac{p}{\rho^* {U_0}^2}$, $\bar{t} = \frac{tU_0}{k}$ allows normalization of the model. Here $M = \frac{6\pi r \mu^*}{m_p}$ is the volume transfer coefficient with an average mass of dust particle m_p and radius r. Hence the term $M\rho_p \frac{(U^* - U_p)}{\rho^*}$ of equation (48) can be written as $\frac{R\,(1+C_s(r_1-1))}{Re(\,1+C_s(r_2-1)\,)}\left(U^* - U_p\right)$. Furthermore $R = \frac{K^* N k^2}{\mu_2}$ is particle concentration parameter and $K^* = 6\pi r \mu_2 U_0$ is the Stokes drag coefficient, N is the number density of particles

per unit volume, and $Re = \frac{\rho_1 U_0}{\mu_1}$ is the Reynolds number. $r_2 = \frac{\mu_2}{\mu_1}$ is the ratio of viscosity, $r_1 = \frac{\rho_2}{\rho_1}$ is the ratio density and $r_4 = \frac{\rho_1 + \rho_2}{\rho_p}$ is the ratio of the density of fluid and dust particles. The body force $F = (\rho^* g + F_s)$ is modeled as gravitation force and interfacial tension by the continuum surface force model, and the surface tension is reconstructed as a volume force $F_s = \sigma\omega\nabla C_i$ where σ is the interfacial tension between two liquid phases and ω is the mean free surface curvature, given by $\omega = -\frac{\nabla^2 C_i}{\|\nabla C_i\|}$ and $Ca = \frac{\mu^* U_0}{\sigma}$ is the capillary number. $Fr = \frac{{U_0}^2}{gk}$ is the Froude number. The time-dependent pressure gradient is applied in the direction of the x-axis for momentum in the averaged flow. As before in schemes I and II, three separate cases for $Ge(t)$ are considered in the computational simulations described later:

Case-I: $Ge(t) = Ge$ (when the flow is induced by applied constant pressure gradient)

Case-II: $Ge(t) = Ge * Sin(wt)$ (when the flow is induced by applied periodic pressure gradient with oscillating parameter w)

Case-III: $Ge(t) = Ge * e^{-\lambda t}$ (when the flow is induced by a decaying pressure gradient with the decaying parameter, λ).

After dropping the bars and introducing the non-dimensional parameters, initial, interfacial, and boundary conditions according to the scheme-III flow the governing equations for fluids and particle-phase equations (36) in the region $(-k \le y \le k)$ emerge as:

$$\frac{\partial C_i}{\partial t} + U^* \frac{\partial C_i}{\partial y} = 0 \qquad (41)$$

$$\frac{\partial U^*}{\partial t} = \frac{Ge(t)}{1 + C_s(r_1 - 1)} + \frac{(1 + C_s(r_2 - 1))}{Re(\,1 + C_s(r_1 - 1)\,)} \frac{\partial^2 U^*}{\partial y^2} - \frac{R\,(1 + C_s(r_2 - 1))}{Re(\,1 + C_s(r_1 - 1)\,)} \left(U^* - U_p\right) + \frac{1}{Fr} - \frac{1 + C_s(r_2 - 1)}{Re * Ca(\,1 + C_s(r_1 - 1)\,)} \frac{\partial^2 C_i}{\partial y^2} \qquad (42)$$

$$\frac{\partial U_p}{\partial t} = \frac{R r_4\,(1 + C_s(r_2 - 1))}{Re(1 + r_1)} \left(U^* - U_p\right) \qquad (43)$$

Initial and boundary conditions are considered as equation (39-40) with $k=1, A_0 = 0.05, B_0 = 2\pi$

3. Numerical solution by modified cubic B-differential quadrature method (MCB-DQM)

To analyze the fluid velocity and temperature distribution for *schemes I and II*, the domain [-1, 1]

is split into [-1, 0] for pure fluid (region –I) and [0, 1] for dusty fluid (region-II). Next both domains are likewise discretized with step length h in the y-(transverse) direction and $\boldsymbol{k'}$in the time scales. Similarly, the domain [-1, 1] is uniformly discretized for flow analysis for scheme III. The nodes are presumed to disperse uniformly.

$a = y_1 < y_2 < \cdots < y < x_n = b$, such that $y_{i+1} - y_i = h$ on the real axis. *(44)*

Following this, let the $R_{i_y}(y_i, t)$ is the first and $R_{i_{yy}}(y_i, t)$ are the second-order derivatives of $U_1(y,t), U_2(y,t), U_P(y,t), T_1(y,t), T_2(y,t), T_P(y,t)\ U^*(y,t), and\ C_s(y,t)$ are obtained at any time on the nodes x_i,

For $= 1,2,3, \dots, n.\ R_{1_y}(y_i, t) = \sum_{j=1}^{N} a^*{}_{ij} R_i(y_j, t)$, *for* $j = 1,2, \dots, N$ *(45)*

$R_{1_{yy}}(y_i, t) = \sum_{j=1}^{N} b^*{}_{ij} R_i(y_j, t)$, *for* $j = 1,2, \dots, N$ *(46)*

Here $a^*{}_{ij}$ $b^*{}_{ij}$are the respective weighting coefficients of first and second-order derivative coefficients concerning y-coordinate, measured using modified cubic B-spline functions. The cubic B-spline functions of the knots are as specified below.

$$\vartheta_j = \frac{1}{h}\begin{cases} (y - y_{j-2})^3, & y\epsilon\ [y_{j-2}, y_{j-1}) \\ (y - y_{j-2})^3 - 4(y - y_{j-1})^3, & y\epsilon [y_{j-1}, y_j) \\ (y_{j+2} - y)^3 - 4(y_{j+1} - y)^3, & y\epsilon\ [y_j, y_{j+1}) \\ (y_{j+2} - y)^3, & y\epsilon [y_{j+1}, y_{j+2}) \\ 0, & otherwise\ . \end{cases} \quad (47)$$

ϑ_j with $j = 0,1,2 \dots, N+1$ forms a basis over the region [a, b].

The updated cubic B-spline functions are described in the nodes as follows.

$\psi_1(y) = \vartheta_1(y) + 2\vartheta_0(y)$ *(48)*

$\psi_2(y) = \vartheta_2(y) - \vartheta_0(y)$ *(49)*

$\psi_j(y) = \vartheta_j, for\ j = 3, \dots . N-2$ *(50)*

$\psi_{N-1}(y) = \vartheta_{N-1}(y) - \vartheta_{N+1}(y)$ *(51)*

$\psi_N(y) = \vartheta_N(y) + 2\vartheta_{N+1}(y)$ *(52)*

Here $\{\psi_1\psi_2,\dots,\psi_N\}$ forms a basis over the region $[a,b]$. Using the modified cubic B-spline function the weighting coefficients are calculated as follows. The first-order derivative approximation is given by:

$$\psi'_k(y_i)=\sum_{j=1}^{N} a^*{}_{ij}\vartheta_k(y_j) \qquad \begin{matrix} for\ i=1,2,\dots,N \\ k=1,2,\dots,N \end{matrix} \tag{53}$$

The estimate can be provided for the *first-knot* point y_1.

$$\psi'_k(y_1)=\sum_{j=1}^{N} a^*{}_{1j}\vartheta_k(y_j) \qquad \begin{matrix} for\ i=1,2,\dots,N \\ k=1,2,\dots,N \end{matrix} \tag{54}$$

Then the tri-diagonal system of equations is formed as

$$\begin{bmatrix} 6 & 1 & 0 & 0 & & & & \\ 0 & 4 & 1 & 0 & \cdots & 0 & & 0 \\ 0 & 1 & 4 & 1 & & & & \\ & \vdots & & 0 & \ddots & 0 & & \vdots \\ & & & & & 1 & 4 & 1 & 0 \\ & 0 & & 0 & \cdots & 0 & 1 & 4 & 0 \\ & & & & & 0 & 0 & 1 & 6 \end{bmatrix} \begin{bmatrix} a^*{}_{11} \\ a^*{}_{12} \\ a^*{}_{13} \\ \cdot \\ \cdot \\ \cdot \\ a^*{}_{N-3} \\ a^*{}_{N-2} \\ a^*{}_{N-1} \\ a^*{}_{N} \end{bmatrix} = \begin{bmatrix} -6/h \\ 6/h \\ 0 \\ \cdot \\ \cdot \\ \cdot \\ 0 \\ 0 \\ 0 \\ 0 \end{bmatrix} \tag{55}$$

Similarly for the point, $y_2$we have $\psi'_k(y_2)=\sum_{j=1}^{N} a^*{}_{2j}\vartheta_k(y_j)$ $\begin{matrix} for\ i=1,2,\dots,N \\ k=1,2,\dots,N \end{matrix}$ *(56)*

Then again, the tri-diagonal system of equations is formed as

$$\begin{bmatrix} 6 & 1 & 0 & 0 & & & & \\ 0 & 4 & 1 & 0 & \cdots & 0 & & 0 \\ 0 & 1 & 4 & 1 & & & & \\ & \vdots & & 0 & \ddots & 0 & & \vdots \\ & & & & & 1 & 4 & 1 & 0 \\ & 0 & & 0 & \cdots & 0 & 1 & 4 & 0 \\ & & & & & 0 & 0 & 1 & 6 \end{bmatrix} \begin{bmatrix} a^*{}_{21} \\ a^*{}_{22} \\ a^*{}_{23} \\ \cdot \\ \cdot \\ \cdot \\ a^*{}_{2N-3} \\ a^*{}_{2N-2} \\ a^*{}_{2N-1} \\ a^*{}_{2N} \end{bmatrix} = \begin{bmatrix} -3/h \\ 0 \\ 3/h \\ 0 \\ \cdot \\ \cdot \\ 0 \\ 0 \\ 0 \\ 0 \end{bmatrix} \tag{57}$$

We continue to find the tri-diagonal systems for the remaining y_i's and the system for last y_N is given by

$$\begin{bmatrix} 6 & 1 & 0 & 0 & & & & & \\ 0 & 4 & 1 & 0 & \cdots & 0 & & 0 & \\ 0 & 1 & 4 & 1 & & & & & \\ & \vdots & & 0 & \ddots & 0 & & \vdots & \\ & & & & & 1 & 4 & 1 & 0 \\ & 0 & & 0 & \cdots & 0 & 1 & 4 & 0 \\ & & & & & 0 & 0 & 1 & 6 \end{bmatrix} \begin{bmatrix} a^*_{N1} \\ a^*_{N2} \\ a^*_{N3} \\ . \\ . \\ . \\ a^*_{NN-3} \\ a^*_{NN-2} \\ a^*_{NN-1} \\ a^*_{NN} \end{bmatrix} = \begin{bmatrix} 0 \\ 0 \\ 0 \\ 0 \\ . \\ . \\ 0 \\ 0 \\ -6/h \\ 6/h \end{bmatrix} \quad (58)$$

The solution of the above systems provides the coefficients, $a^*_{11}, a^*_{12} \dots, a^*_{1N}$, $a^*_{21}, a^*_{22} \dots, a^*_{2N} \dots, a^*_{N1}, a^*_{N2} \dots, a^*_{NN}$. Then the values of b^*_{ij} for $i = 1,2,3 \dots N, j = 1,2,3 \dots N$ are calculated as follows

$$b^*_{ij} = \begin{Bmatrix} 2a^*_{ij}\left(a^*_{ij} - \frac{1}{y_i - y_j}\right) & \text{for } i \neq j \\ -\sum_{i=1, i\neq j}^{N} b^*_{ij} & i = j \end{Bmatrix} \quad (59)$$

reduced system of ordinary differential equations in time, that is, represented as for i=1, 2, 3…, N.$V_t = R(U_1, U_2, T_1, T_2, U_p, T_p U^* C_i)$ *(60)*

The system is solved by the following scheme.

$$V_1 = U_0 + \frac{\Delta t}{2} * R(U_1, U_2, T_1, T_2, U_p, T_p U^* C_i) \quad (61)$$

$$V_2 = U_1 + \frac{\Delta t}{2} * R(U_1, U_2, T_1, T_2, U_p, T_p U^* C_i) \quad (62)$$

$$V_3 = \frac{2U_0}{3} + \frac{U_1}{3} + \frac{\Delta t}{6} * R\left(U_1, U_2, T_1, T_2, U_p, T_p U^* C_i\right) \quad (63)$$

$$V_M = U_3 + \frac{\Delta t}{2} * R(U_1, U_2, T_1, T_2, U_p, T_p U^* C_i) \quad (64)$$

4. MCB-DQM Results and Analysis

Under three separate flow schemes, the unidirectional unstable Generalized Couette flow of two immiscible dusty and pure fluids attributable to the time-dependent pressure gradient is examined. To pursue the solutions, traditional no-slip and hyper-stick conditions are assumed at the boundaries. First, the obtained numerical results are validated for the velocity profile of single non-dusty Newtonian fluid flow (Here in the absence of dust particle the Stokes drag coefficient $K^* = 0$ and particle concentration parameter $R = 0$ and r_1=1, r_2=1) by comparing them with the exact solutions of Poiseuille flow (*Ge*=10) through a horizontal channel. It is observed from Table 1-3

that a good agreement is seen as the maximum absolute error and root mean square error is very less between the calculated numerical solution and the exact solution. As the number of discretizing nodes ($N = 31 - 201$) and time ($t = 0.1 - 2$) is increasing the errors are also reducing so it can be noticed that the applied modified cubic B-spline differential quadrature method is suitable for the current system of fluid flow.

The two-fluid flow coupled problem in the corresponding regions with stable interfaces through separate schemes I, II and have been numerically solved, and velocity, temperature profiles of fluids, and dust particles have been obtained. Single mean flow problems with inconsistent interfaces under scheme III have also been addressed and the interface reconstruction profiles have been acquired along with averaged flow and dust particles velocity profiles. The results are discussed in the following set of fixed values of all parameters, *Ge*=10, *Re*=2, *R*=0.5, r_1=0.5, r_2=0.5, r_4=200, C_s=0.5, Ca=0.5, $Fr = 2, \lambda = 1, w = 2$.

4.1. Results and analysis of immiscible dusty and pure fluid flow under the scheme-I

Figure 2(a-g) shows the velocity profiles in dusty and pure fluid areas and *Figure 2(h-o)* exhibits the dust particle velocity with Reynolds numbers, particulate concentration parameters, applied pressure gradients, density ratio, viscosity ratio, and time. It is found that the velocity profiles for dust particles and fluids in both regions are parabolic and because the lower fluid is more viscous and denser than the upper one (r_1=0.5,r_2=0.5), the curvature of pure fluid velocity is lower than the dusty fluid profile. *Figure 2(a)* exhibits the change in fluid velocities and *Figure 2(h)* shows the particle velocities with varying times when a constant pressure gradient is applied. It is noted that, with rising time, the fluids and particle velocities are growing in respective regions, and at a higher time, it may become stable. The fluid velocities $Figure\ 2\ (b)$ and dust particle velocity $Figure\ 2\ (i)$ are pulsating, wherein the flow is caused by the periodic pressure gradient and never attains the steady-state. Hence the velocities increase when $0 < \omega t \leq \frac{\pi}{2}$, decrease when $\frac{\pi}{2} < \omega t \leq \frac{3\pi}{2}$ and further increase with $\frac{3\pi}{2} < \omega t \leq \frac{5\pi}{2}$. $Figure\ 2\ (c\ and\ j)$ reveals that the fluid velocities in both the regions and particle velocity in the upper region decrease with time and eventually attain a steady-state as time is enhanced, for the case where periodic pressure gradient induces the flow. It is also worth mentioning that, owing to the upper plate movement (the generalized Couette flow), the velocities do not approach zero with time. It may be observed from $Figure\ 2\ (d -$

$for\ fluid\ velocity$) and $Figure\ 2\ (n - particle\ velocity)$ that the increase in Reynolds number enhances the fluids and particle velocities for all three cases of applied constant, periodic, and decaying pressure gradients, which is due to the elevation in inertial (momentum) force relative to viscous hydrodynamic force. However, the variations are larger in magnitude in the dusty fluid region than the pure fluid (Newtonian) region indicating a greater sensitivity in the velocity of the particles compared to the Newtonian fluid. It can be noted from $Figure\ 2(\ g\ and\ o)$ that the velocity magnitudes of fluid and particle are accentuated with an increment of the pressure gradient. An increase in the ratios of viscosities $r_2$and densities r_1 corresponds to an increase in the viscosity and density of the *dusty fluid* region relative to the pure Newtonian fluid region. Because of this for all three applied pressure gradients, a significant decline in dust particle and fluid velocity is observed in Region-II whereas no tangible change in the pure fluid velocity in Region-I is witnessed with an increase in the ratio r_2 and r_1 see $Figure\ 2\ (e\ and\ f)$ for fluid velocities and $Figure\ 2\ (k\ and\ l)$ for particle velocities. *Figure 2 (m)* indicates that the dust particle velocity increases with an enhancement of particle concentration parameter, and no variation in fluid velocities are observed for all three pressure gradients hence the figures are not mentioned.

Figure 3 (A-H) illustrates the evolution in the fluid and dust particle temperature distributions, in the respective dusty and pure fluid regions with numerous thermophysical parameters. *Figure 3 (A-C)* demonstrate that the dust particles and fluid temperatures in respective regions increase with progression in time and elevation in Eckert number Ec and the ratio of viscosities r_2. Clearly, a greater proportion of kinetic energy is converted to thermal energy via internal friction with increment in Eckert number - this boosts the temperature magnitudes. A decrement in temperature magnitudes is observed with an increase in Reynolds number Re and Prandtl number p_r – clearly greater inertial effect and smaller thermal diffusivity (and thermal conductivity) manifest in suppression in thermal diffusion in the regime and lower temperatures are computed see *Figure 3 (D-E).* However, owing to the momentum transfer near the interface, the profiles show the opposite trend since temperature apparently is elevated weakly in both the regions. It can be deduced from *Figure 3 (F-G)* that the pure fluids do not display any notable displacement in the temperature profiles with an increase in the parameter K_r and C_r in region-I. Conversely, the temperatures are significantly increased in region II as a parameter K_r increases whereas a significant decline are computed as parameter C_r increases for both dust particles and fluid. Similarly, the variation in the

temperature profiles is only observed in region II (See *Figure 2 (H)* with an increase in the particle concentration parameter$R$ .A slight decrease in the dusty fluid and a significant increase in the particle temperature profiles can be seen. This means the increasing presence of dust particles therefore also weakly inhibits thermal diffusion in the dual fluid regime.

The skin friction coefficient is a dimensionless quantity that describes the amount of resistance provided to an object moving through a fluid and causing skin friction drift on the surface. Table 4 shows that skin friction increases with *time* and *Reynolds number* at the lower plate of the channel, but remains constant with increasing values of *particle concertation parameter*, the *ratio of viscosities and densities* $(R, r_2, r_1, and\ r_3)$. On the upper plate, the decrease in skin friction co-efficient is induced by rising values of time, $Re, and\ r_3$. When r_1, r_2 is increased, the co-efficient improves and it does not change with R.

The Nusselt number (*Nu*) is the ratio of convective heat transfer to conductive heat transfer at the boundary. Table 5 shows that the Nusselt number increases at the upper plate and decrease at the lower plate with *time, Reynolds number, particle concertation parameter* R, *ratio of viscosities and densities* $(r_1, r_2, and\ r_3)$.

4.2 Results and analysis of immiscible dusty and pure fluid flow under the scheme-II

$Figure\ 4\ (a-f)$ visualize the response in fluid and dust particle velocities under scheme-II with selected thermophysical parameters. In both regions generally, it is apparent that owing to the uniform suction effect, the velocity profiles of dust and fluids are not parabolic, and the curvature of pure fluid velocity is markedly different from the dusty fluid velocity topology. It is also observed that under scheme-II, the flow profiles are elongated as compared to the flow profiles under scheme-I. $Figure\ 4(a)$ exhibits the change in fluid and particle velocities with varying times when a constant pressure gradient is applied. It is noted that, with rising time, the fluid velocity is clearly increasing in both regions *i. e. a substantial acceleration is induced*. However, the magnitude of velocity profiles computed by periodic pressure *is lower than* decaying and constant pressure gradients see *Figure 4(c).* It can be noted from *Figure 4(b)* the velocity profiles increase with the increment of the pressure gradient again owing to the imparting of momentum to the channel flow regime. It is observed from *Figure 4(d)* that augmentation in Reynolds number enhances the fluids and particle velocities for all three cases of applied constant, periodic, and decaying pressure gradients. However, the variations are more extensive in magnitude in the dusty

fluid region compared to the pure fluid region. *Figure 4(e)* shows that owing to the suction effect (removal of material via the boundary) for *all three applied pressure gradient cases*, the dust particle and fluids velocities climb significantly in the region -II and decline slightly in the region-I with an increase in the density ratio r_1. A weak decline in the pure fluid region for fluid velocity profiles can be seen in *Figure 4(f)* and the profiles exhibit an increasing nature in the pure fluid region *but only near the interface in the dusty fluid region*. The qualitative properties of fluids and particle temperature profiles under Scheme - I and II are equivalent and therefore these results are not presented for brevity.

4.3 Interface tracking under scheme-III

Figure 5 shows the evolution of the interface between the two liquid zones with varying time and amplitude under Scheme III when the constant pressure gradient is present, and a vertical shift can be seen in the interface. It is also observed that initially, the vertical elongation of the interface is large, and thereafter the shape of the interface evolves progressively over time; hence the undulating sequence occurs faster for a more considerable time. It is also judicious to note that the top fluid is less viscous than the bottom fluid. It is also noticed that the qualitative characteristics of this flow shall be maintained, and as expected, the interface starts to shift vertically if the amplitude is enhanced. The two liquids do not penetrate each other in the same way. Hence it can be concluded that initially at small times, a large sinusoidal interface is observed, and later, the peak of the wave progresses rapidly as time increases. It is also worth mentioning that the evolution of the interface profile for periodic and decaying pressure gradient cases is qualitatively similar to that computed for the constant pressure gradient case, although magnitudes are different (for brevity these simulations are not visualized).

Table 1: Numerical vs Exact solution for N=31, t=0.1

Exact	Numerical	Error
1.00000	1.00000	0.00000
0.87307	0.87330	0.00023
0.75169	0.75215	0.00047
0.64116	0.64181	0.00065
0.54631	0.54713	0.00082
0.47129	0.47226	0.00096
0.41938	0.42046	0.00107
0.39285	0.39400	0.00115
0.39285	0.39405	0.00120
0.41938	0.42061	0.00123
0.47129	0.47252	0.00122
0.54631	0.54751	0.00120
0.64116	0.64232	0.00116
0.75169	0.75280	0.00112
0.87307	0.87413	0.00106
1.00000	1.00100	0.00100
1.12693	1.12786	0.00093
1.24831	1.24919	0.00087
1.35884	1.35966	0.00082
1.45369	1.45445	0.00076
1.52871	1.52942	0.00072
1.58062	1.58130	0.00068
1.60715	1.60780	0.00064
1.60715	1.60776	0.00061
1.58062	1.58120	0.00058
1.52871	1.52925	0.00055
1.45369	1.45420	0.00051
1.35884	1.35931	0.00047
1.24831	1.24872	0.00041
1.12693	1.12731	0.00038
1.00000	1.00000	0.00000
Maximum Error =0.0012 RMSE=0.00083205		

Table 2: Numerical vs Exact solution for N=62, t=0.5

Exact	Numerical	Error	Exact	Numerical	Error
5.00000	5.00000	0.00000	5.00437	5.00510	0.00073
4.99128	4.99156	0.00028	5.01305	5.01378	0.00073
4.98265	4.98296	0.00031	5.02160	5.02231	0.00072
4.97421	4.97455	0.00034	5.02992	5.03062	0.00071
4.96604	4.96641	0.00037	5.03792	5.03861	0.00070
4.95823	4.95863	0.00040	5.04551	5.04620	0.00068
4.95086	4.95129	0.00043	5.05263	5.05330	0.00067
4.94402	4.94447	0.00045	5.05919	5.05984	0.00065
4.93776	4.93824	0.00048	5.06512	5.06576	0.00064
4.93217	4.93268	0.00051	5.07036	5.07098	0.00062
4.92730	4.92783	0.00053	5.07486	5.07545	0.00060
4.92319	4.92375	0.00056	5.07856	5.07914	0.00058
4.91990	4.92048	0.00058	5.08143	5.08198	0.00056
4.91746	4.91806	0.00060	5.08343	5.08397	0.00054
4.91590	4.91652	0.00062	5.08455	5.08507	0.00052
4.91522	4.91587	0.00064	5.08478	5.08527	0.00049
4.91545	4.91611	0.00066	5.08410	5.08457	0.00047
4.91657	4.91725	0.00068	5.08254	5.08298	0.00044
4.91857	4.91927	0.00069	5.08010	5.08052	0.00042
4.92144	4.92215	0.00070	5.07681	5.07720	0.00039
4.92514	4.92586	0.00072	5.07270	5.07307	0.00037
4.92964	4.93036	0.00073	5.06783	5.06817	0.00034
4.93488	4.93561	0.00073	5.06224	5.06255	0.00031
4.94081	4.94155	0.00074	5.05598	5.05627	0.00029
4.94737	4.94811	0.00075	5.04914	5.04940	0.00026
4.95449	4.95523	0.00075	5.04177	5.04200	0.00023
4.96208	4.96283	0.00075	5.03396	5.03416	0.00020
4.97008	4.97083	0.00075	5.02579	5.02596	0.00017
4.97840	4.97915	0.00075	5.01735	5.01749	0.00014
4.98695	4.98769	0.00075	5.00872	5.00884	0.00012
4.99563	4.99637	0.00074	5.00000	5.00000	0.00000
Maximum Error = 0.00075002 RMSE= 0.00055847					

Table 3: Error with time and discretizing points

	For N=51, t=0.5	For N=101, t=1	For N=151, t=1.5	For N=201, t=2
MAX ERROR	0.000749	0.000481	0.000341	0.000320
RMSE	0.000557	0.000377	0.000280	0.000229

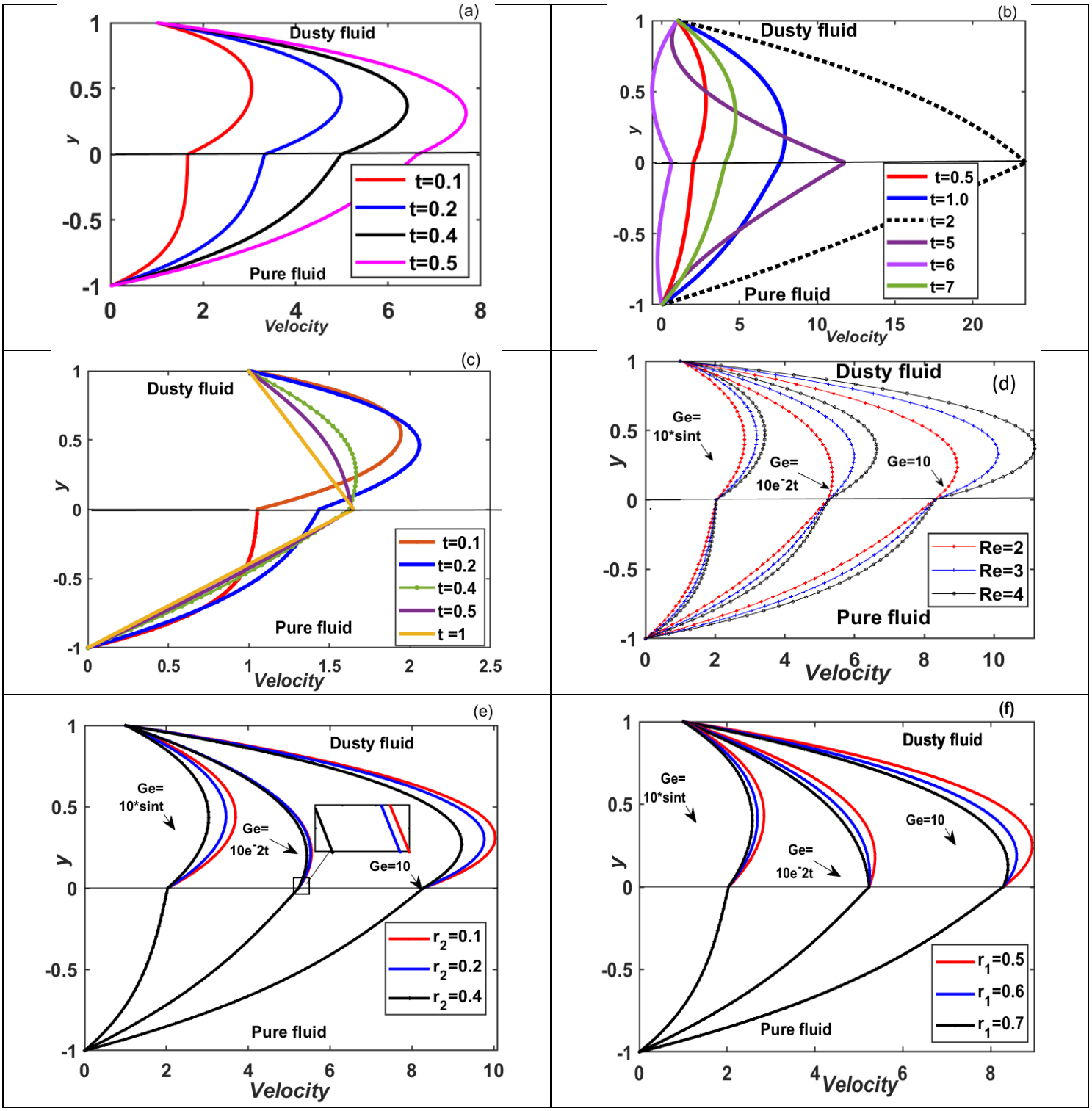
(a)
Dusty fluid
Pure fluid
t=0.1
t=0.2
t=0.4
t=0.5
y
Velocity
(b)
Dusty fluid
Pure fluid
t=0.5
t=1.0
t=2
t=5
t=6
t=7
y
Velocity
(c)
Dusty fluid
Pure fluid
t=0.1
t=0.2
t=0.4
t=0.5
t =1
y
Velocity
(d)
Dusty fluid
Ge= 10*sint
Ge= 10e^-2t
Ge=10
Re=2
Re=3
Re=4
Pure fluid
y
Velocity
(e)
Dusty fluid
Ge= 10*sint
Ge= 10e^-2t
Ge=10
r2=0.1
r2=0.2
r2=0.4
Pure fluid
y
Velocity
(f)
Dusty fluid
Ge= 10*sint
Ge= 10e^-2t
Ge=10
r1=0.5
r1=0.6
r1=0.7
Pure fluid
y
Velocity

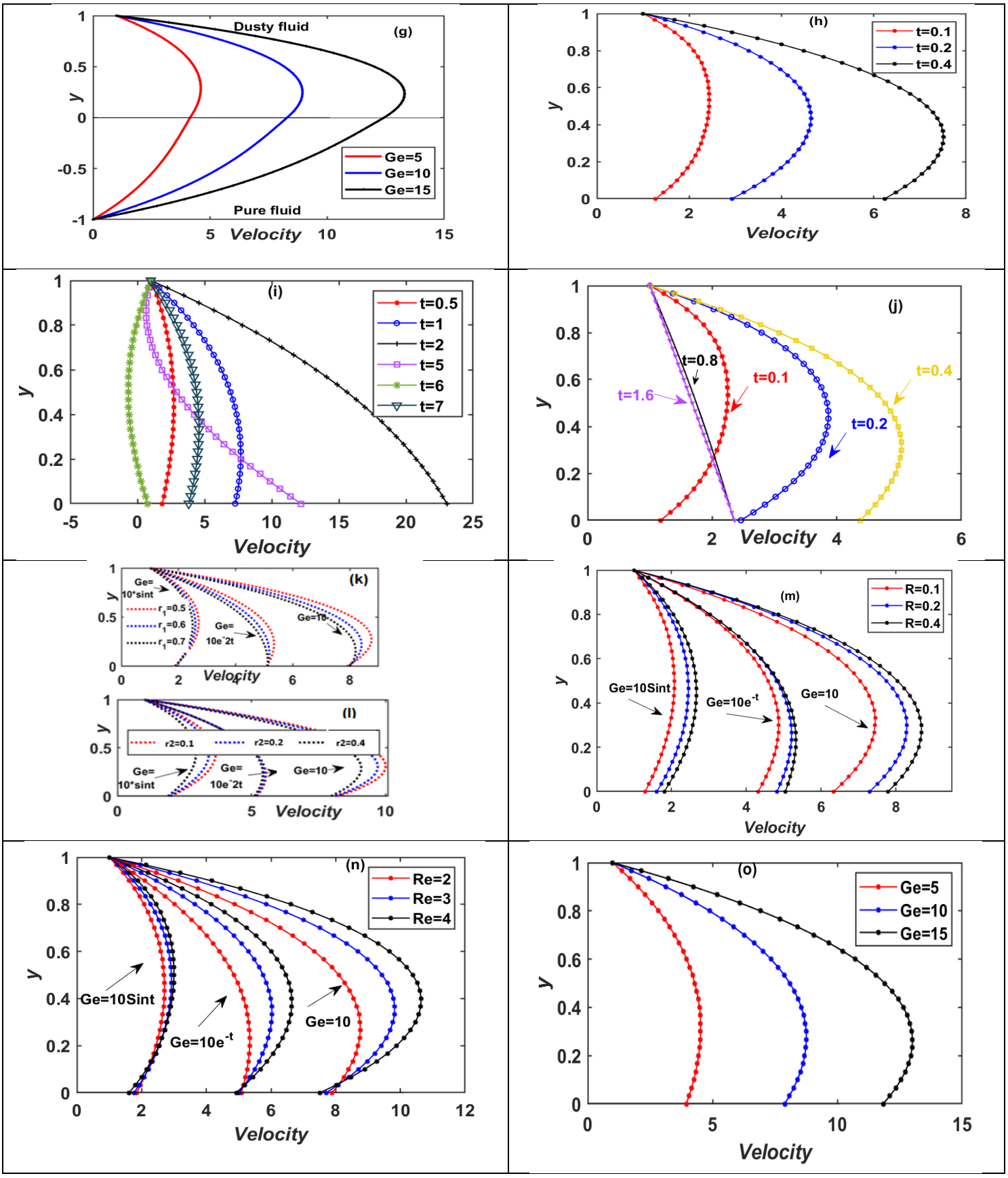

Figure 2: Velocity profiles with varying parameters under scheme-I

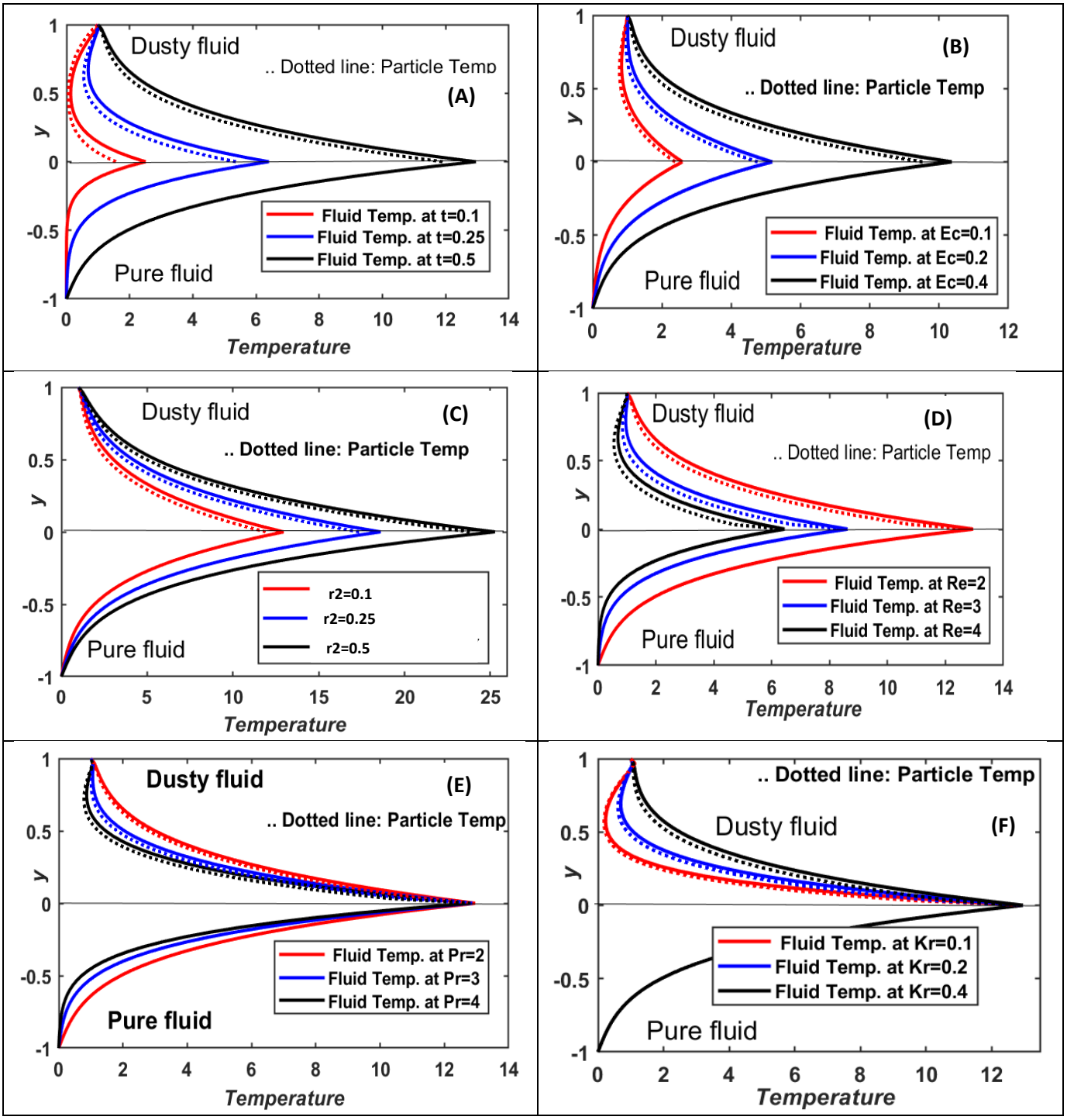
Dusty fluid
.. Dotted line: Particle Temp
(A)
Fluid Temp. at t=0.1
Fluid Temp. at t=0.25
Fluid Temp. at t=0.5
Pure fluid
y
Temperature
Dusty fluid
(B)
.. Dotted line: Particle Temp
Fluid Temp. at Ec=0.1
Fluid Temp. at Ec=0.2
Fluid Temp. at Ec=0.4
Pure fluid
Temperature
Dusty fluid
(C)
.. Dotted line: Particle Temp
r2=0.1
r2=0.25
r2=0.5
Pure fluid
Temperature
Dusty fluid
(D)
.. Dotted line: Particle Temp
Fluid Temp. at Re=2
Fluid Temp. at Re=3
Fluid Temp. at Re=4
Pure fluid
Temperature
Dusty fluid
(E)
.. Dotted line: Particle Temp
Fluid Temp. at Pr=2
Fluid Temp. at Pr=3
Fluid Temp. at Pr=4
Pure fluid
Temperature
.. Dotted line: Particle Temp
Dusty fluid
(F)
Fluid Temp. at Kr=0.1
Fluid Temp. at Kr=0.2
Fluid Temp. at Kr=0.4
Pure fluid
Temperature

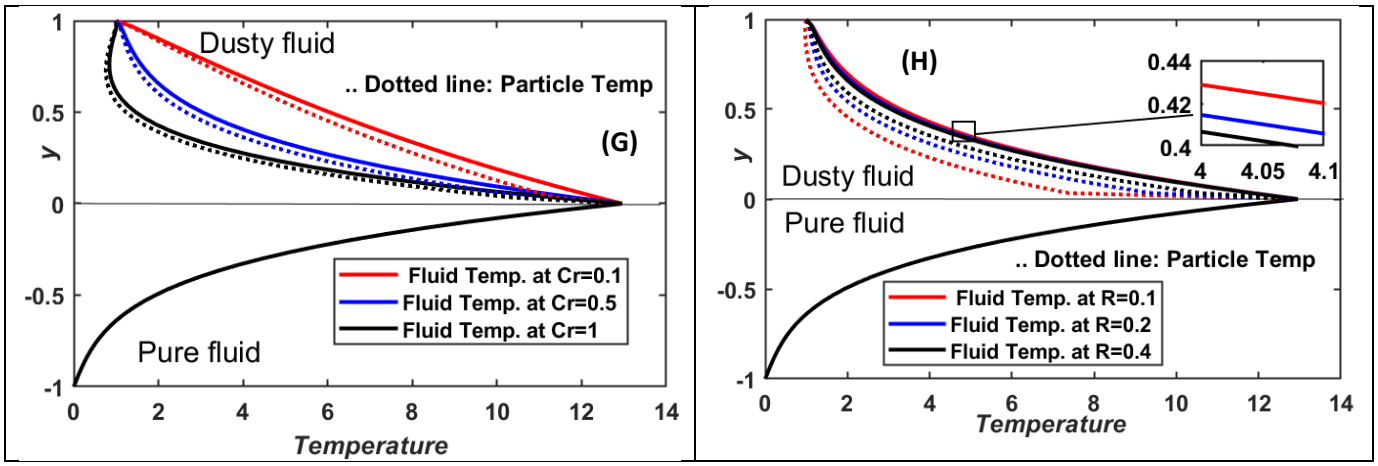

Figure3: Temperature profiles with varying parameters under scheme-I

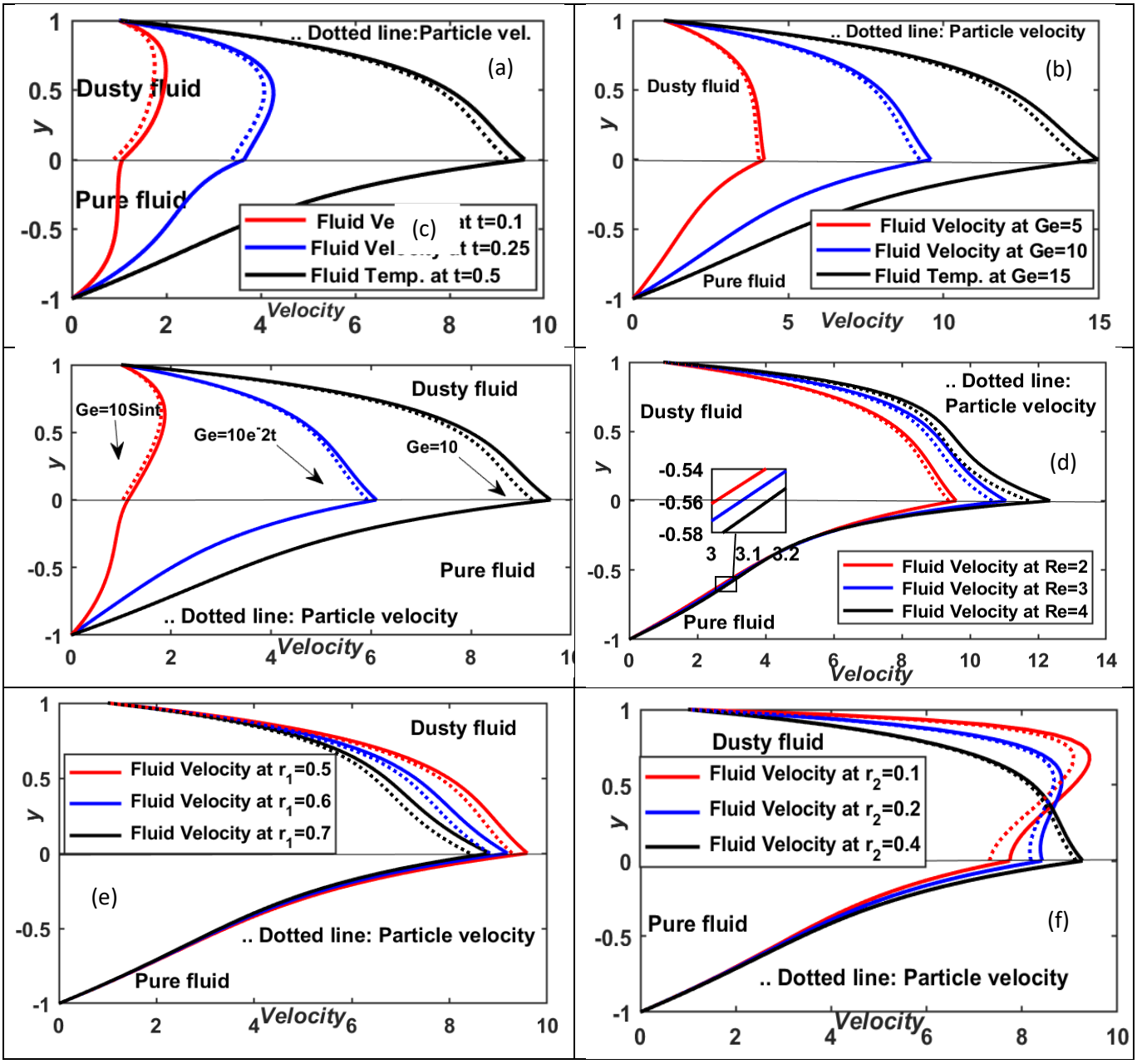

Figure 4: Velocity profiles with varying parameters under scheme-II.

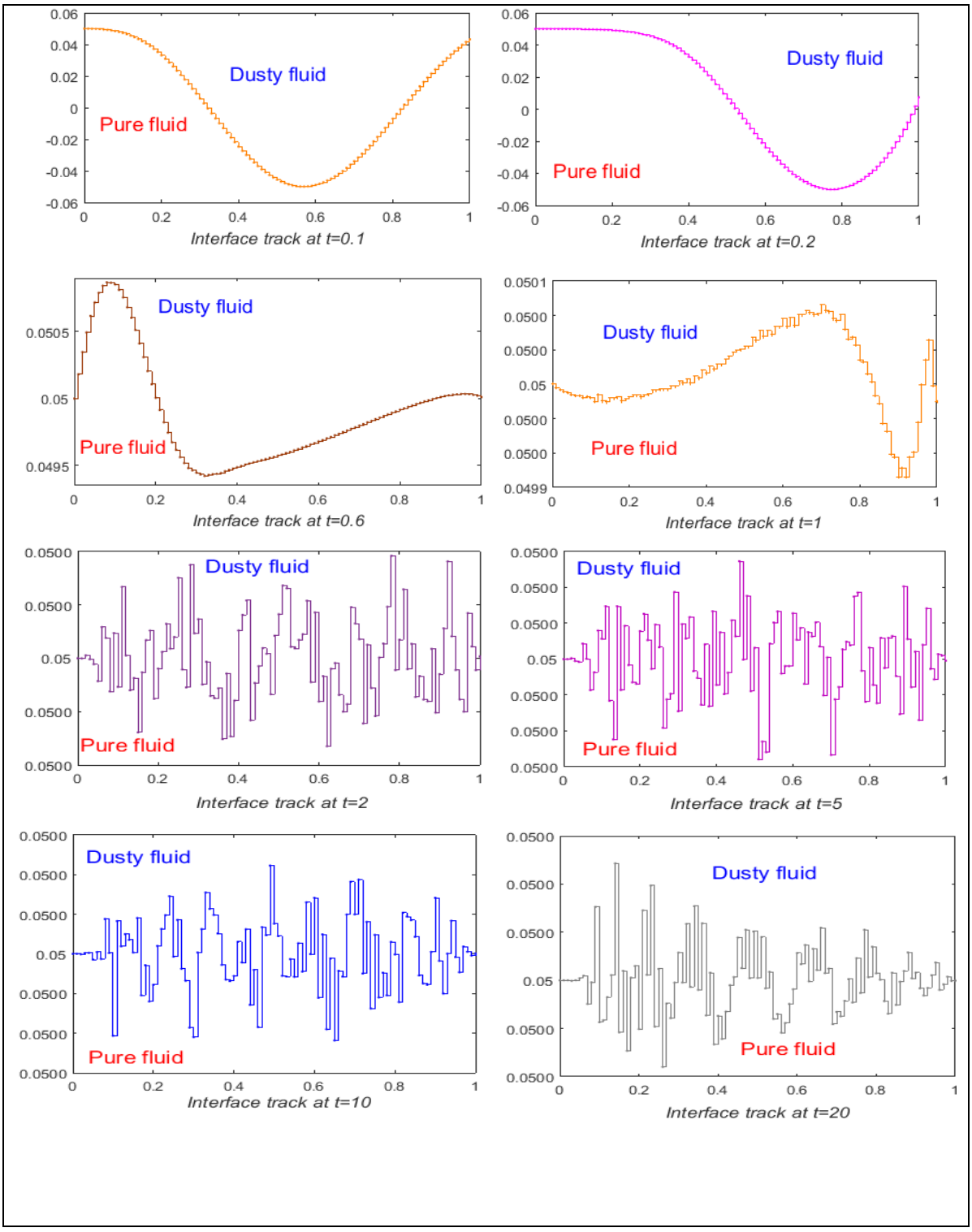
Dusty fluid
Pure fluid
Interface track at t=0.1
Dusty fluid
Pure fluid
Interface track at t=0.2
Dusty fluid
Pure fluid
Interface track at t=0.6
Dusty fluid
Pure fluid
Interface track at t=1
Dusty fluid
Pure fluid
Interface track at t=2
Dusty fluid
Pure fluid
Interface track at t=5
Dusty fluid
Pure fluid
Interface track at t=10
Dusty fluid
Pure fluid
Interface track at t=20

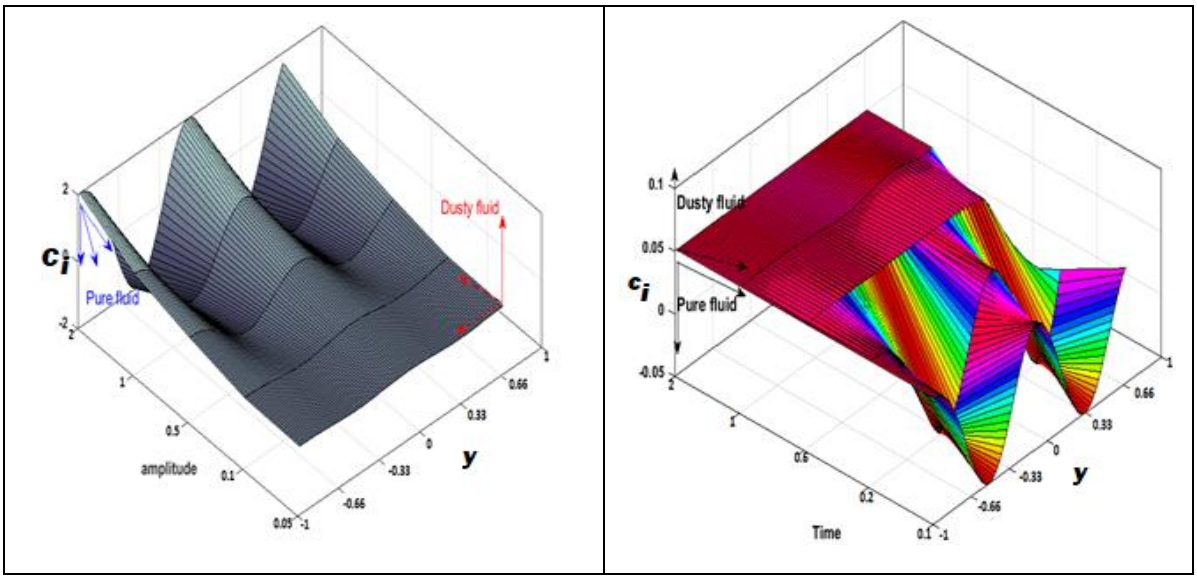

Figure 5: Sequence of interface position with varying time under the scheme III **Note** - the horizontal axis is magnified from 0 to 1 to show the details.

Table 4:Skin friction Coefficient with varying parameter

T	Lower plate	Upper plate		Re	Lower plate	Upper plate		R	Lower plate	Upper plate
0.1	4.955721	-7.36259		2	4.955721	-7.36259		0.3	4.955721	-7.36354
0.2	7.046197	-12.1264		3	6.057319	-8.99958		0.5	4.955721	-7.36259
0.3	8.651487	-15.2324		4	6.980517	-10.3652		1	4.955721	-7.36219
0.4	10.01278	-17.4958		5	7.789845	-11.5605		2	4.955721	-7.362
r1	Lower plate	Upper plate		r2	Lower plate	Upper plate		r3	Lower plate	Upper plate
0.3	4.955721	-11.5605		0.5	4.955721	-7.36259		50	4.955721	-7.30038
0.5	4.955721	-9.47826		0.6	4.955721	-6.25616		100	4.955721	-7.3294
0.8	4.955721	-8.22539		0.7	4.955721	-5.35892		200	4.955721	-7.35322
1	4.955721	-7.36259		0.8	4.955721	-4.60702		400	4.955721	-7.37042

Table 5: Nusselt number with varying parameter

Re	Lower plt	Upper plt		t	Lower plt	Upper plt		Kr	Lower plt	Upper plt		r2	Lower plt	Upper plt
2	-0.00231	2.913626		0.1	-0.00231	5.827251		0.1	-0.00231	11.85818		0.5	-0.00231	5.827251
3	-1.19E-05	6.171196		0.2	-0.89595	11.55846		0.3	-0.00231	7.680487		0.6	-0.00243	9.352168
4	-2.25E-06	7.261058		0.3	-8.06006	29.57051		0.5	-0.00231	2.913626		0.7	-0.00254	11.56419
5	-2.22E-06	7.671225		0.4	-26.5908	62.88988		0.7	-0.00231	-1.80442		0.8	-0.00263	12.97823
Pr	Lower plt	Upper plt		Ec	Lower plt	Upper plt		r1	Lower plt	Upper plt				
2	-0.00231	5.827251		0.25	-0.00116	1.392961		0.25	-0.00069	0.951823				
3	-1.67E-05	20.68563		0.5	-0.00231	5.827251		0.5	-0.00231	5.827251				
4	-5.28E-06	35.045		0.75	-0.00347	10.26154		0.75	-0.00459	12.10357				
5	-6.60E-06	49.13418		1	-0.00462	14.69583		1	-0.00724	37.73138				

6. Conclusions

The unsteady Generalized Couette flow of two immiscible dusty and pure fluids through a horizontal channel under three distinct scenarios with a stable and unstable interface has been analyzed numerically using the modified Cubic B-Spine Differential Quadrature method (MCB-DQM). The effects of the emerging thermophysical and hydrodynamic parameters on fluid and particle velocity, flow velocity, temperature, and interface evolution have been addressed. The core findings of the present analysis can be summarized in the following points:

a) For the flow under schemes, I and II an increasingly oscillatory and decreasing behavior in the fluids velocities and particle velocity with time is computed in the respective regions I and II when the flow is induced by constant, periodic, and decaying pressure gradients respectively.

b) As anticipated in the stable interface schemes flow, values of the fluids and particle-phase velocities are enhanced with increment in the pressure gradient.

c) -Increasing Reynolds number in the stable interface schemes generates a marked enhancement in the fluid and particle-phase velocities for all three applied constant, periodic, and decaying pressure gradient cases. However, in the case of periodic gradient under scheme-II, the velocities are observed to be decreasing near the interface.

d) Elevation in the particle concentration parameter increases the velocities of dust particles with all three applied pressure gradient scenarios, in the stable interface schemes.

e) An increment in the ratio of densities, in the case of all three applied pressure gradients, is found to significantly damp the velocities in the dusty fluid regions for schemes I, II. Furthermore, elevation in density ratio depresses velocities slightly for scheme II but does not tangibly modify the velocities in Scheme I flow in the pure (Newtonian) fluid region.

f) Under scheme-I, a significant decline in dust particle and fluid velocities in the dusty fluid region and a negligible decline in the pure fluid velocity is noted with an increase in the ratio of viscosities for all three applied pressure gradients.

g) Under the Scheme –II flow, the behavior of fluids and particle velocities for the periodic pressure gradient differs from the constant and decaying pressure gradient case with an increment in the ratio of viscosities. The velocity profiles decline in both the regions when the periodic pressure gradient is applied while the pure fluid velocity increases weakly for both constant and decaying applied pressure gradients and additionally the dusty fluid and

particle velocity alter from decreasing to increasing trends near the interface. The dissimilar behavior observed may be owing to the suction effect and coupling nature of fluids.

The qualitative features of fluids and particle temperature profiles under scheme-I and II are similar about all control parameters. Hence the key output for temperature can be summarized as follows:

a) Dust particle and fluid temperatures in respective regions increase with an enhancement in time, Eckert number, and the ratio of viscosities (i.e. heating of the channeling regime) whereas they decrease with Reynolds number and Prandtl number (i.e. cooling of the channeling regime). Temperatures decline slightly in both regions with an increase in particle concentration parameters.
b) A rise in the ratio of densities results in a substantial decline in dust particle and fluid temperature in region-II, and pure fluid temperature decreases slightly in region-I; however, owing to the momentum transfer near the interface, the profiles show the converse response and temperatures are slightly enhanced in both regions.
c) Elevation in the ratio of thermal conductivities produces a notable enhancement in temperature magnitudes of both dust particles and fluid in region II: however, the pure fluids do not exhibit any shift in the temperature.
d) A boost in the ratio of specific heat of both fluids induces a major reduction in the temperature magnitudes of both dust particles and fluid in region II: nevertheless, the pure fluids do not demonstrate any displacement in the temperature.
e) Under the scheme-III, tracking the interface between the two immiscible liquids is also simulated with varying times. It is noticed that initially, the vertical elongation of the interface is large, and subsequently, the topology evolves with time. Therefore, the undulating sequence occurs faster for a more considerable time, and the qualitative features of this flow are retained with high time and amplitude.

The MCB-DQM algorithm described offers excellent capabilities in interfacial fluid dynamics. The present study has of course neglected electrically conducting properties of either dusty or Newtonian fluids. These give rise to magnetohydrodynamic behavior and this may be assessed in future work.

References

1. G. F. Carrier, Shock waves in a dusty gas, *J. Fluid Mechanics*, 4 (4), 376 – 382 (1958).

2. L. Massimilla *et al*., Flow of fluid-particle suspensions from liquid-fluidized beds, *Ind. Eng. Chem. Fundamen.* 2, 3, 194–199 (1963).
3. K.K. Sankara and L.V.K.V. Sarma, On the steady flow produced in fluid-particle suspension by an infinite rotating disk with surface suction, *Int. J. Eng. Sci*., 23 (1985) 875-886.
4. M.S. Alam Sarker, Effect of Coriolis force on vorticity covariance in MHD turbulent flow of dusty fluid, *Int. J. Energy Research*, 21, 1399-1403 (1997).
5. O. Igra *et. al.,* Dusty gas flow in a converging-diverging nozzle, *ASME J. Fluids Eng*. 121(4): 908–913 (1999).
6. D.H. Michael, The steady motion of a sphere in a dusty gas, *J. Fluid Mechanics*, 31 (1), 175-192 (1968).
7. K. Tseronis *et al.,* Modelling mass transport in solid oxide fuel cell anodes: a case for a multidimensional dusty gas-based model, *Chemical Engineering Science, 63 (23)* 5626-5638 (2008).
8. P.G. Saffman, On the stability of laminar flow of a dusty gas, *J. Fluid Mechanics*, 13, 120-128 (1962).
9. F. Marble, Dynamics of Dusty Gases, *Annual Review of Fluid Mechanics*, 2: 397-446 (1970).
10. R. Duraiswami, A. Prosperetti, Linear pressure waves in fogs, *Journal of Fluid Mechanics*, 299, 187-215 (2006).
11. A. Chauvière and J. Chaskalovic, Dusty debris in tornadoes modelled by high Reynolds number two cells vortices, *International Journal of Engineering Science*, 43, 1486-1497 (2005).
12. M. A. Allaham and J. Peddieson , The flow induced by a rotating disk in a particulate suspension, *International Journal of Engineering Science*, 31, 1025-1034 (1993).
13. S. V. Manuilovich, Dusty-gas flow in a channel with horizontal walls, *Fluid Dynamics*, **47**, 84–100 (2012).
14. M. Bilal *et al.,* Couette flow of viscoelastic dusty fluid in a rotating frame along with the heat transfer, *Scientific Reports*, 11, Article number: 506 (2021).
15. A.N. Osiptsov, Mathematical modeling of dusty-gas boundary layers, *Appl. Mech. Rev*. 50(6), 357–370 (1997).
16. Debnath, L. & Ghosh, A. K. On unsteady hydromagnetic flows of a dusty fluid between two oscillating plates. *Appl. Sci. Res.* **45**(4), 353–365 (1988).
17. Dey, D. Dusty hydromagnetic Oldroyd fluid flow in a horizontal channel with volume fraction and energy dissipation. *Int. J. Heat Technol.* **34**(3), 415–422 (2010).
18. N. Datta *et al.,* Unsteady heat transfer to pulsatile flow of a dusty viscous incompressible fluid in a channel, *International Journal of Heat and Mass Transfer*, 36, 1783-1788 (1993).
19. K. Vajravelu *et al.,* Hydromagnetic fluid flow and heat transfer at a stretching sheet with fluid-particle suspension and variable fluid properties**,** *ASME J. Fluids Eng*.135(1): 011101 (2013).
20. S.K. Kumar *et al.,* Fluid-particle suspension flow past a stretching sheet, *Int. J. Engineering Science*, 29, 123-132 (1991).
21. D.C. Dalal *et al.,* Unsteady natural convection of a dusty fluid in an infinite rectangular channel, *Int. J. Heat Mass Transfer*, 41, 547-562 (1998).
22. W. Gretler and R. Regenfelder, Variable-energy blast waves generated by a piston moving in a dusty gas, *J. Engineering Mathematics*, 52, 321–336 (2005).
23. M. Saqib *et al*., Generalized magnetic blood flow in a cylindrical tube with magnetite dusty particles, *Journal of Magnetism and Magnetic Materials*, 484, 490-496 (2019).

24. H.M. Park and D.E. Rosner, Combined inertial and thermophoretic effects on particle deposition rates in highly loaded dusty-gas systems, C*hemical Engineering Science, 44,* 2233-2244 (1989).
25. H.S. Takhar *et al.,* Unsteady MHD flow of a dusty viscous liquid in a rotating channel with Hall currents, *Int J Energy Research*, 17 (1) 69-74 (1993).
26. [26] A.J. Chamkha, Analytical solutions for flow of a dusty fluid between two porous flat plates, *ASME J. Fluids Eng*., 116(2): 354–356 (1994).
27. O. Anwar Bég, H. S. Takhar, T. A. Bég, R. Bharagava, Rawat, S, Nonlinear Magneto-heat transfer in a fluid-particle suspension flowing via a non-Darcian channel with heat source and buoyancy effects: Numerical Study, *J. Engineering Sciences*, 19, 1, 63-88 (2008).
28. S. Mukhopadhyay *et al.,* Numerical study of concentrated fluid–particle suspension flow in a wavy channel, *Int. J. Energy Research*, 59 (10) 1125-1155 (2009).
29. T. A. Bég, M.M. Rashidi, O. Anwar Bég and N. Rahimzadeh, Differential transform semi-numerical simulation of biofluid-particle suspension flow and heat transfer in non-Darcian porous media, *Computer Methods Biomechanics Biomedical Engineering*, 16(8): 896-907 (2013).
30. G. Palani *et al.,* Free convection of a dusty-gas flow along a semi-infinite vertical cylinder, *Int J Num Meth Fluids*, 63 (4), 517-532 (2010).
31. A.T. Corey, *Mechanics of Immiscible Fluids in Porous Media*, Water Resources Publications, LLC, Colorado, USA (2012).
32. B. J.Briscoe *et al.,* A review of immiscible fluid mixing, *Advances in Colloid and Interface Science, 81,* 1-17 (1999).
33. G. Yorshiaki *et al.,* Experiments and MPS analysis of stratification behavior of two immiscible fluids, *Nuclear Engineering and Design*, 265, 210-221 (2013).
34. S. Jachalski *et al*., Impact of interfacial slip on the stability of liquid two-layer polymer films, *J. Engineering Mathematics,* 86, 9-29 (2014).
35. D. Nikodijević *et al.,* Flow and heat transfer of two immiscible fluids in the presence of uniform inclined magnetic field, *Math. Prob. Engineering*, Volume 2011 |Article ID 132302 | https://doi.org/ 10.1155/2011/132302
36. M. Mori *et al.,* A finite element analysis of a free surface drainage problem of two immiscible fluids, *Int. J. Num. Meth Fluids*, 9, 569-582 (1989).
37. H. Tang and L.C. Wrobel, Modelling the interfacial flow of two immiscible liquids in mixing processes, *Int. J. Engineering Science,* 43, 1234-1256 (2005).
38. T. wan et al., A hybrid scheme based on finite element/volume methods for two immiscible fluid flows, *Int J Num Meth Fluids,* 61 (8) 930-949 (2009).
39. P.T. Than *et al.,* Instability of Poiseuille flow of two immiscible liquids with different viscosities in a channel, *Int. J. Engineering Science,* 25, 189-204 (1987).
40. A.A. Yagodnitsyna, Flow patterns of immiscible liquid-liquid flow in a rectangular microchannel with T-junction, *Chemical Engineering Journal, 303,* 547-554 (2016).
41. O. Anwar Bég, A. Zaman, N. Ali, S.A. Gaffar and Eemaan T. A. Bég, Numerical computation of oscillatory two-immiscible magnetohydrodynamic flow in a dual porous media system: FTCS and FEM study, *Heat Transfer*, 48, 1-19 (2019). DOI: 10.1002/htj.21429
42. Y. Zhou *et al.,* MLPG_R method for modelling 2D flows of two immiscible fluids, *Int. J. Num. Meth Fluids*, 84, 385-408 (2017).
43. McLean RH, Manry CW, Whitaker WW (1966) Displacement mechanics in primary cementing, *Society of Petroleum Engineers*, USA, paper number SPE 1488.

44. Bittleston SH, Ferguson J and Frigaard IA (2002). Mud removal and cement placement during primary cementing of an oil well; laminar non-Newtonian displacements in an eccentric annular Hele-Shaw cell. *J Engng. Math* 43: 229–253.
45. H. Tang *et al.,* Tracking of immiscible interfaces in multiple material mixing processes, *Computational Materials Science, 29,* 103-118 (2004).
46. A. Borrelli, G. Giantesio, and M. C. Patria, "Reverse flow in magnetoconvection of two immiscible fluids in a vertical channel," *J. Fluids Eng. Trans. ASME,* 2017, doi: 10.1115/1.4036670.
47. W. Tauber, S. O. Unverdi, and G. Tryggvason, "The nonlinear behavior of a sheared immiscible fluid interface," *Phys. Fluids*, 2002, doi: 10.1063/1.1485763.
48. J.C. Umavathi and O. Anwar Bég, Effects of thermophysical properties on heat transfer at the interface of two immiscible fluids in a vertical duct: numerical study, *Int. J. Heat Mass Transfer,* 154 (2020). 119613 (18 pages)
49. C.S. Yih, "Instability due to viscosity stratification," *J. Fluid Mech.*, 1967, doi: 10.1017/S0022112067000357.
50. B. Dong, Y. Y. Yan, W. Li, and Y. Song, "Lattice Boltzmann simulation of viscous fingering phenomenon of immiscible fluids displacement in a channel," *Comput. Fluids*, 2010, doi: 10.1016/j.compfluid.2009.12.005.
51. R. B. DeBar, "Fundamentals of the KRAKEN code," *Tech. Rep.*, 1974.
52. D. L. Youngs, "Time-dependent multi-material flow with large fluid distortion.," *Numerical Methods in Fluid Dynamics (pp.273-285), Editors: K. W. Morton and M. J. Baines, Academic Press, New York, USA,* 1982.
53. J. Li, "Calcul d'Interface Affine par Morceaux," *Comptes Rendus - Academie des Sciences, Serie II: Mecanique, Physique, Chimie, Astronomie*. 1995.
54. V. R. Gopala and B. G. M. van Wachem, "Volume of fluid methods for immiscible-fluid and free-surface flows," *Chem. Eng. J.*, 2008, doi: 10.1016/j.cej.2007.12.035.
55. M. M. Bhatti, A. Riaz, L. Zhang, S. M. Sait, and R. Ellahi, "Biologically inspired thermal transport on the rheology of Williamson hydromagnetic nanofluid flow with convection: an entropy analysis," *J. Therm. Anal. Calorim.*, 2021, doi: 10.1007/s10973-020-09876-5.
56. K. L. Hsiao, "Micropolar nanofluid flow with MHD and viscous dissipation effects towards a stretching sheet with multimedia feature," *Int. J. Heat Mass Transf.*, 2017, doi: 10.1016/j.ijheatmasstransfer.2017.05.042.
57. L. Zhang, M. M. Bhatti, M. Marin, and K. S. Mekheimer, "Entropy analysis on the blood flow through anisotropically tapered arteries filled with magnetic zinc-oxide (ZnO) nanoparticles," *Entropy*, 2020, doi: 10.3390/E22101070.
58. R. E. Abo-Elkhair, M. M. Bhatti, and K. S. Mekheimer, "Magnetic force effects on peristaltic transport of hybrid bio-nanofluid (Au–Cu nanoparticles) with moderate Reynolds number: An expanding horizon," *Int. Commun. Heat Mass Transf.*, 2021, doi: 10.1016/j.icheatmasstransfer.2021.105228.
59. K. L. Hsiao, "To promote radiation electrical MHD activation energy thermal extrusion manufacturing system efficiency by using Carreau-Nanofluid with parameters control method,"

Energy, 2017, doi: 10.1016/j.energy.2017.05.004.

60. M. Bibi, A. Zeeshan, and M. Y. Malik, “Numerical analysis of unsteady flow of three-dimensional Williamson fluid-particle suspension with MHD and nonlinear thermal radiations,” *Eur. Phys. J. Plus*, 2020, doi: 10.1140/epjp/s13360-020-00857-z.
61. M. Bibi, A. Zeeshan, M. Y. Malik, and K. U. Rehman, “Numerical investigation of the unsteady solid-particle flow of a tangent hyperbolic fluid with variable thermal conductivity and convective boundary,” *Eur. Phys. J. Plus*, 2019, doi: 10.1140/epjp/i2019-12651-9.
62. K. L. Hsiao, “Stagnation electrical MHD nanofluid mixed convection with slip boundary on a stretching sheet,” *Appl. Therm. Eng.*, 2016, doi: 10.1016/j.applthermaleng.2015.12.138.
63. K. L. Hsiao, “Combined electrical MHD heat transfer thermal extrusion system using Maxwell fluid with radiative and viscous dissipation effects,” *Appl. Therm. Eng.*, 2017, doi: 10.1016/j.applthermaleng.2016.08.208.
64. S. Haider, N. Ijaz, A. Zeeshan, and Y. Z. Li, “Magneto-hydrodynamics of a solid-liquid two-phase fluid in rotating channel due to peristaltic wavy movement,” *Int. J. Numer. Methods Heat Fluid Flow*, 2020, doi: 10.1108/HFF-02-2019-0131.
65. G. Tryggvason *et al.*, “A Front-Tracking Method for the Computations of Multiphase Flow,” *J. Comput. Phys.*, 2001, doi: 10.1006/jcph.2001.6726.
66. A. Riaz and H. A. Tchelepi, “Numerical simulation of immiscible two-phase flow in porous media,” *Phys. Fluids*, 2006, doi: 10.1063/1.2166388.
67. M. Devakar and A. Raje, “A study on the unsteady flow of two immiscible micropolar and Newtonian fluids through a horizontal channel: A numerical approach,” *Eur. Phys. J. Plus*, 2018, doi: 10.1140/epjp/i2018-12011-5.
68. R. Bellman, B. G. Kashef, and J. Casti, “Differential quadrature: A technique for the rapid solution of nonlinear partial differential equations,” *J. Comput. Phys.*, 1972, doi: 10.1016/0021-9991(72)90089-7.
69. J. R. Quan and C. T. Chang, “New insights in solving distributed system equations by the quadrature method-II. Numerical experiments,” *Comput. Chem. Eng.*, 1989, doi: 10.1016/0098-1354(89)87043-7.
70. J. R. Quan and C. T. Chang, “New insights in solving distributed system equations by the quadrature method-I. Analysis,” *Comput. Chem. Eng.*, 1989, doi: 10.1016/0098-1354(89)85051-3.
71. C. Shu and B. E. Richards, “Application of generalized differential quadrature to solve two-dimensional incompressible Navier-Stokes equations,” *Int. J. Numer. Methods Fluids*, 1992, doi: 10.1002/fld.1650150704.
72. F. Civan, “Comment on ‘application of generalized quadrature to solve two-dimensional incompressible Navier–Stokes equations’, By C. Shu and B. E. Richards,” *International Journal for Numerical Methods in Fluids*. 1993, doi: 10.1002/fld.1650171007.
73. C. Shu, Y. Y. Shan, and N. Qin, “Development of a local MQ-DQ-based stencil adaptive method and its application to solve incompressible Navier-Stokes equations,” *Int. J. Numer. Methods Fluids*, 2007, doi: 10.1002/fld.1467.

74. Y. Y. Shan, C. Shu, and Z. L. Lu, "Application of local MQ-DQ method to solve 3D incompressible viscous flows with curved boundary," *C. - Comput. Model. Eng. Sci.*, 2008, doi: 10.3970/cmes.2008.025.099.
75. R. Jiwari and A. S. Alshomrani, "A new algorithm based on modified trigonometric cubic B-splines functions for nonlinear Burgers'-type equations," *Int. J. Numer. Methods Heat Fluid Flow*, 2017, doi: 10.1108/HFF-05-2016-0191.
76. Geeta Arora, V. Joshi, and R. C. Mittal, "Numerical simulation of nonlinear Schrödinger equation in one and two dimensions," *Math. Model. Comput. Simulations*, 2019, doi: 10.1134/S2070048219040070.
77. R. C. Mittal and R. K. Jain, "Numerical solutions of nonlinear Burgers' equation with modified cubic B-splines collocation method," *Appl. Math. Comput.*, 2012, doi: 10.1016/j.amc.2012.01.059.
78. K. Ramesh and V. Joshi, "Numerical solutions for unsteady flows of a magnetohydrodynamic jeffrey fluid between parallel plates through a porous medium," *Int. J. Comput. Methods Eng. Sci. Mech.*, 2019, doi: 10.1080/15502287.2018.1520322.
79. R. Katta, R. K. Chandrawat, and V. Joshi, "A Numerical study of the unsteady flow of two immiscible micropolar and Newtonian fluids through a horizontal channel using DQM with B-Spline basis function," in *Journal of Physics: Conference Series*, 2020, doi: 10.1088/1742-6596/1531/1/012090
80. K. Ramesh, D. Tripathi, O. Anwar Bég, A. Kadir, Slip and Hall current effects on viscoelastic fluid-particle suspension flow in a peristaltic hydromagnetic blood micropump, *Iranian Journal of Science and Technology, Transactions of Mechanical Engineering (2018). doi.org/10.1007/s40997-018-0230-5 (18 pages)*
81. S. I. Abdelsalam, M. M. Bhatti, A. Zeeshan, A. Riaz and O. Anwar Bég, Metachronal propulsion of magnetized particle-fluid suspension in a ciliated channel with heat and mass transfer, *Physica Scripta*, 94, 115301 (13pp) (2019).
82. H. A. Attia, W. Abbas, and M. A. M. Abdeen, "Ion slip effect on unsteady Couette flow of a dusty fluid in the presence of uniform suction and injection with heat transfer," *J. Brazilian Soc. Mech. Sci. Eng.*, 2016, doi: 10.1007/s40430-015-0311-y.
83. J. Li and Y. Renardy, "Numerical study of flows of two immiscible liquids at low Reynolds number," *SIAM Rev.*, 2000, doi: 10.1137/S0036144599354604.

APPENDIX

1. A-1. Numerical solution of immiscible dusty and pure fluids flow under the scheme-I.

To get the velocity and temperature profile of dusty and pure fluid flow under scheme-I, one replaces the approximation of the spatial components of the first and second-order obtained by using MCB-DQM. Hence the system of coupled partial equations (22-27) followed by *scheme I, numerically* solved with the initial and boundary conditions equation (19-20). and the velocities temperature profiles of both fluids and particles are obtained. The equations (22-27) can be updated as

Region-I ($-k \leq y \leq 0$) (Pure fluid region):

$$v_{1_t} = Ge(t) + \frac{\sum_{j=1}^{N} b^*_{ij} v_1(y_j,t)}{Re} \quad (1.1)$$

$$T_{1_t} = \frac{\sum_{j=1}^{N} b^*_{ij} T_1(y_j,t)}{Re*Pr} + \frac{Ec}{Re}\left(\sum_{j=1}^{N} a^*_{ij} v_1(y_j,t)\right)^2 \quad (1.2)$$

Region-II (0 ≤ y ≤ k) (Dusty fluid):

$$v_{2_t} = \frac{Ge(t)}{r_2} + \frac{r_1}{r_2}\frac{\sum_{j=1}^{N} b^*_{ij} v_2(y_j,t)}{Re} - \frac{R*r_1}{r_2}\frac{\left(v_2(y_j,t) - v_P(y_j,t)\right)}{Re} \quad (1.3)$$

$$v_{p_t} = \frac{R*r_3*r_1}{r_2}\frac{\left(v_2(y_j,t) - v_P(y_j,t)\right)}{Re} \quad (1.4)$$

$$T_{2_t} = \frac{\boldsymbol{k_r}*\sum_{j=1}^{N} b^*_{ij} T_2(y_j,t)}{\boldsymbol{C_r}*r_2*Re*Pr} + \frac{r_1}{\boldsymbol{C_r}*r_2}\frac{Ec}{Re}\left(\sum_{j=1}^{N} a^*_{ij} v_2(y_j,t)\right)^2 + \frac{2}{3}\frac{R*\boldsymbol{k_r}}{\boldsymbol{C_r}*r_1*pr}\frac{\left(T_p(y_j,t) - T_2(y_j,t)\right)}{Re} + \frac{R*r_3*r_1}{r_2}\frac{\left(v_2(y_j,t) - v_P(y_j,t)\right)^2}{Re} \quad (1.5)$$

$$T_{p_t} = \frac{2}{3}\frac{R*\boldsymbol{k_r}*\boldsymbol{C_{r_r}}*r_3}{\boldsymbol{C_r}*r_1*pr}\frac{\left(T_2(y_j,t) - T_p(y_j,t)\right)}{Re} \quad (1.5a)$$

Thus, equations *(1.1-1.5)* are reduced into a system of ordinary differential equations in time, that is, for *i=1, 2, 3…, N*, and the system is solved by four-stage order three SSP RK43 scheme. The velocities and temperature in both regions are obtained as follows:

At the first stage for *i=1,2,3…,n*:

Region-I ($-k \le y \le 0$) (Pure fluid region):

$$v_{1_1} = v_{1_0} + \frac{\Delta t}{2}\left(Ge(t) + \frac{\sum_{j=1}^{N} b^*_{ij} v_{1_0}(y_j,t)}{Re}\right) \quad (1.6)$$

$$T_{1_1} = T_{1_0} + \frac{\Delta t}{2}\left(\frac{\sum_{j=1}^{N} b^*_{ij} T_{1_0}(y_j,t)}{Re*Pr} + \frac{Ec}{Re}\left(\sum_{j=1}^{N} a^*_{ij} v_{1_0}(y_j,t)\right)^2\right) \quad (1.7)$$

Region-II (0 ≤ y ≤ k) (Dusty fluid):

$$v_{2_1} = v_{2_0} + \frac{\Delta t}{2}\left(\frac{Ge(t)}{r_2} + \frac{r_1}{r_2}\frac{\sum_{j=1}^{N} b^*_{ij} v_{2_0}(y_j,t)}{Re} - \frac{R*r_1}{r_2}\frac{\left(v_{2_0}(y_j,t) - v_{P_0}(y_j,t)\right)}{Re}\right) \quad (1.8)$$

$$v_{p_1} = v_{P_0} + \frac{\Delta t}{2}\left(\frac{R*r_3*r_1}{r_2}\frac{\left(v_{2_0}(y_j,t) - v_{P_0}(y_j,t)\right)}{Re}\right) \quad (1.9)$$

$$T_{2_1} = T_{2_0} + \frac{\Delta t}{2}\left(\begin{array}{l}\frac{\boldsymbol{k_r}*\sum_{j=1}^{N} b^*_{ij} T_{2_0}(y_j,t)}{\boldsymbol{C_r}*r_2*Re*Pr} + \frac{r_1}{\boldsymbol{C_r}*r_2}\frac{Ec}{Re}\left(\sum_{j=1}^{N} a^*_{ij} v_{2_0}(y_j,t)\right)^2 + \\ \frac{2}{3}\frac{R*\boldsymbol{k_r}}{\boldsymbol{C_r}*r_1*pr}\frac{\left(T_{P_0}(y_j,t) - T_{2_0}(y_j,t)\right)}{Re} + \frac{R*r_3*r_1}{r_2}\frac{\left(v_{2_0}(y_j,t) - v_{P_0}(y_j,t)\right)^2}{Re}\end{array}\right) \quad (1.20)$$

$$T_{P_1} = T_{P_0} + \frac{\Delta t}{2}\left(\frac{2}{3}\frac{R*\boldsymbol{k_r}*\boldsymbol{C_{r_r}}*r_3}{\boldsymbol{C_r}*r_1*pr}\frac{\left(T_{2_0}(y_j,t) - T_{P_0}(y_j,t)\right)}{Re}\right) \quad (1.21)$$

At the first stage of the scheme, the initial and boundary conditions (19-20) are considered accordingly.

At the second stage for *i=1,2,3…,n:*

Region-I ($-k \le y \le 0$) (Pure fluid region):

$$\upsilon_{1_2} = \upsilon_{1_1} + \frac{\Delta t}{2}\left(Ge(t) + \frac{\sum_{j=1}^{N} b^*_{ij}\upsilon_{1_1}(y_j,t)}{Re}\right) \quad (1.22)$$

$$T_{1_2} = T_{1_1} + \frac{\Delta t}{2}\left(\frac{\sum_{j=1}^{N} b^*_{ij}T_{1_1}(y_j,t)}{Re*Pr} + \frac{Ec}{Re}\left(\sum_{j=1}^{N} a^*_{ij}\upsilon_{1_1}(y_j,t)\right)^2\right) \quad (1.23)$$

Region-II (0 ≤ y ≤ k) (Dusty fluid):

$$\upsilon_{2_2} = \upsilon_{2_1} + \frac{\Delta t}{2}\left(\frac{Ge(t)}{r_2} + \frac{r_1}{r_2}\frac{\sum_{j=1}^{N} b^*_{ij}\upsilon_{2_1}(y_j,t)}{Re} - \frac{R*r_1}{r_2}\frac{\left(\upsilon_{2_1}(y_j,t)-\upsilon_{P_1}(y_j,t)\right)}{Re}\right) \quad (1.24)$$

$$\upsilon_{p_2} = \upsilon_{P_1} + \frac{\Delta t}{2}\left(\frac{R*r_3*r_1}{r_2}\frac{\left(\upsilon_{2_1}(y_j,t)-\upsilon_{P_1}(y_j,t)\right)}{Re}\right) \quad (1.25)$$

$$T_{2_2} = T_{2_1} + \frac{\Delta t}{2}\left(\begin{array}{l}\frac{\boldsymbol{k_r}*\sum_{j=1}^{N} b^*_{ij}T_{2_1}(y_j,t)}{\boldsymbol{C_r}*r_2*Re*Pr} + \frac{r_1}{\boldsymbol{C_r}*r_2}\frac{Ec}{Re}\left(\sum_{j=1}^{N} a^*_{ij}\upsilon_{2_1}(y_j,t)\right)^2 + \\ \frac{2}{3}\frac{R*\boldsymbol{k_r}}{\boldsymbol{C_r}*r_1*pr}\frac{\left(T_{P_1}(y_j,t)-T_{2_1}(y_j,t)\right)}{Re} + \frac{R*r_3*r_1}{r_2}\frac{\left(\upsilon_{2_1}(y_j,t)-\upsilon_{P_1}(y_j,t)\right)^2}{Re}\end{array}\right) \quad (1.26)$$

$$T_{P_2} = T_{P_1} + \frac{\Delta t}{2}\left(\frac{2}{3}\frac{R*\boldsymbol{k_r}*\boldsymbol{C_{r_r}}*r_3}{\boldsymbol{C_r}*r_1*pr}\frac{\left(T_{2_1}(y_j,t)-T_{P_1}(y_j,t)\right)}{Re}\right) \quad (1.27)$$

At the second stage of the scheme, the initial and boundary conditions (19-20)are considered accordingly.

At the third stage for *i=1,2,3…,n:*

Region-I ($-k \le y \le 0$) (Pure fluid region):

$$\upsilon_{1_3} = \frac{2\upsilon_{1_0}}{3} + \frac{\upsilon_{1_2}}{3} + \frac{\Delta t}{6}\left(Ge(t) + \frac{\sum_{j=1}^{N} b^*_{ij}\upsilon_{1_2}(y_j,t)}{Re}\right) \quad (1.28)$$

$$T_{1_3} = \frac{2T_{1_0}}{3} + \frac{T_{1_2}}{3} + \frac{\Delta t}{6}\left(\frac{\sum_{j=1}^{N} b^*_{ij}T_{1_2}(y_j,t)}{Re*Pr} + \frac{Ec}{Re}\left(\sum_{j=1}^{N} a^*_{ij}\upsilon_{1_2}(y_j,t)\right)^2\right) \quad (1.29)$$

Region-II (0 ≤ y ≤ k) (Dusty fluid):

$$\upsilon_{2_3} = \frac{2\upsilon_{2_0}}{3} + \frac{\upsilon_{2_2}}{3} + \frac{\Delta t}{6}\left(\frac{Ge(t)}{r_2} + \frac{r_1}{r_2}\frac{\sum_{j=1}^{N} b^*_{ij}\upsilon_{2_2}(y_j,t)}{Re} - \frac{R*r_1}{r_2}\frac{\left(\upsilon_{2_2}(y_j,t)-\upsilon_{P_2}(y_j,t)\right)}{Re}\right) \quad (1.30)$$

$$\upsilon_{p_3} = \frac{2\upsilon_{P_0}}{3} + \frac{\upsilon_{P_2}}{3} + \frac{\Delta t}{6}\left(\frac{R*r_3*r_1}{r_2}\frac{\left(\upsilon_{2_2}(y_j,t)-\upsilon_{P_2}(y_j,t)\right)}{Re}\right) \quad (1.31)$$

$$T_{2_3} = \frac{2T_{2_0}}{3} + \frac{T_{2_2}}{3} + \frac{\Delta t}{6}\left(\begin{array}{l}\frac{\boldsymbol{k_r}*\sum_{j=1}^{N} b^*_{ij}T_{2_2}(y_j,t)}{\boldsymbol{C_r}*r_2*Re*Pr} + \frac{r_1}{\boldsymbol{C_r}*r_2}\frac{Ec}{Re}\left(\sum_{j=1}^{N} a^*_{ij}\upsilon_{2_2}(y_j,t)\right)^2 + \\ \frac{2}{3}\frac{R*\boldsymbol{k_r}}{\boldsymbol{C_r}*r_1*pr}\frac{\left(T_{P_2}(y_j,t)-T_{2_2}(y_j,t)\right)}{Re} + \frac{R*r_3*r_1}{r_2}\frac{\left(\upsilon_{2_2}(y_j,t)-\upsilon_{P_2}(y_j,t)\right)^2}{Re}\end{array}\right) \quad (1.32)$$

$$T_{P_3} = \frac{2T_{P_0}}{3} + \frac{T_{P_2}}{3} + \frac{\Delta t}{6}\left(\frac{2}{3}\frac{R*\boldsymbol{k_r}*\boldsymbol{C_{r_r}}*r_3}{\boldsymbol{C_r}*r_1*pr}\frac{\left(T_{2_2}(y_j,t)-T_{P_2}(y_j,t)\right)}{Re}\right) \quad (1.33)$$

At the third stage of the scheme, the initial and boundary conditions (19-20)are considered accordingly.

At the *fourth stage* for *i=1,2,3…,n*:

Region-I ($-k \le y \le 0$) (Pure fluid region):

$$v_1 = v_{1_3} + \frac{\Delta t}{2}\left(Ge(t) + \frac{\sum_{j=1}^{N} b^*_{ij} v_{1_3}(y_j,t)}{Re}\right) \quad (1.34)$$

$$T_1 = T_{1_3} + \frac{\Delta t}{2}\left(\frac{\sum_{j=1}^{N} b^*_{ij} T_{1_3}(y_j,t)}{Re*Pr} + \frac{Ec}{Re}\left(\sum_{j=1}^{N} a^*_{ij} v_{1_3}(y_j,t)\right)^2\right) \quad (1.35)$$

Region-II for Dusty fluid ($0 \le y \le k$):

$$v_2 = v_{2_3} + \frac{\Delta t}{2}\left(\frac{Ge(t)}{r_2} + \frac{r_1}{r_2}\frac{\sum_{j=1}^{N} b^*_{ij} v_{2_3}(y_j,t)}{Re} - \frac{R*r_1}{r_2}\frac{\left(v_{2_3}(y_j,t) - v_{P_3}(y_j,t)\right)}{Re}\right) \quad (1.36)$$

$$v_p = v_{P_3} + \frac{\Delta t}{2}\left(\frac{R*r_3*r_1}{r_2}\frac{\left(v_{2_3}(y_j,t) - v_{P_2}(y_j,t)\right)}{Re}\right) \quad (1.37)$$

$$T_2 = T_{2_3} + \frac{\Delta t}{2}\left(\begin{array}{l} \frac{\boldsymbol{k_r}*\sum_{j=1}^{N} b^*_{ij} T_{2_3}(y_j,t)}{\boldsymbol{C_r}*r_2*Re*Pr} + \frac{r_1}{\boldsymbol{C_r}*r_2}\frac{Ec}{Re}\left(\sum_{j=1}^{N} a^*_{ij} v_{2_3}(y_j,t)\right)^2 + \\ \frac{2}{3}\frac{R*\boldsymbol{k_r}}{\boldsymbol{C_r}*r_1*pr}\frac{\left(T_{P_3}(y_j,t) - T_{2_3}(y_j,t)\right)}{Re} + \frac{R*r_3*r_1}{r_2}\frac{\left(v_{2_3}(y_j,t) - v_{P_3}(y_j,t)\right)^2}{Re} \end{array}\right) \quad (1.38)$$

$$T_P = T_{P_3} + \frac{\Delta t}{2}\left(\frac{2}{3}\frac{R*\boldsymbol{k_r}*\boldsymbol{C_{r_r}}*r_3}{\boldsymbol{C_r}*r_1*pr}\frac{\left(T_{2_3}(y_j,t) - T_{P_3}(y_j,t)\right)}{Re}\right) \quad (1.39)$$

At the fourth stage of the scheme, the initial and boundary conditions *(19-20)* are considered accordingly. Hence the fluid velocity, temperature profiles v_1, T_1 of pure fluid in the region-I and fluid, particle velocity, and temperature profiles $v_2,\ v_P, T_2, T_P$ of dusty fluid in the region-II have been numerically obtained in the fourth stage of MCB-DQM.

2. *A-2. Numerical solution of immiscible dusty and pure fluids flow under the scheme-II.*

To get the velocity and temperature profile of dusty and pure fluid flow under scheme-II, replace the approximation of the spatial components of the first and second-order obtained by using MCB-DQM. Hence the system of coupled partial equations *(29-34)* followed by *scheme II* is updated as equation *(2.1-2.6)* then solved numerically, and the velocity and temperature profiles of both fluids and particles are obtained.

Region-I ($-k \le y \le 0$) (Pure fluid region):

$$v_{1_t} = Ge(t) + \frac{\sum_{j=1}^{N} b^*_{ij} v_1(y_j,t)}{Re} - S_1\left(\sum_{j=1}^{N} a^*_{ij} v_1(y_j,t)\right) \quad (2.1)$$

$$T_{1_t} = \frac{\sum_{j=1}^{N} b^*_{ij} T_1(y_j,t)}{Re*Pr} + \frac{Ec}{Re}\left(\sum_{j=1}^{N} a^*_{ij} v_1(y_j,t)\right)^2 - S_1\left(\sum_{j=1}^{N} a^*_{ij} T_1(y_j,t)\right) \quad (2.2)$$

Region-II ($0 \le y \le k$) (Dusty fluid):

$$v_{2_t} = \frac{Ge(t)}{r_2} + \frac{r_1}{r_2}\frac{\sum_{j=1}^{N} b^*_{ij} v_2(y_j,t)}{Re} - \frac{R*r_1}{r_2}\frac{\left(v_2(y_j,t) - v_P(y_j,t)\right)}{Re} - S_2\left(\sum_{j=1}^{N} a^*_{ij} v_2(y_j,t)\right) \quad (2.3)$$

$$v_{p_t} = \frac{R*r_3*r_1}{r_2}\frac{\left(v_2(y_j,t)-v_P(y_j,t)\right)}{Re} \tag{2.4}$$

$$T_{2_t} = \frac{\boldsymbol{k_r}*\sum_{j=1}^{N} b^*{}_{ij}T_2(y_j,t)}{\boldsymbol{C_r}*r_2*Re*Pr} + \frac{r_1}{\boldsymbol{C_r}*r_2}\frac{Ec}{Re}\left(\sum_{j=1}^{N} a^*{}_{ij}v_2(y_j,t)\right)^2 + \frac{2}{3}\frac{R*\boldsymbol{k_r}}{\boldsymbol{C_r}*r_1*pr}\frac{\left(T_p(y_j,t)-T_2(y_j,t)\right)}{Re}$$

$$+ \frac{R*r_3*r_1}{r_2}\frac{\left(v_2(y_j,t)-v_P(y_j,t)\right)^2}{Re} - S_2\left(\sum_{j=1}^{N} a^*{}_{ij}T_2(y_j,t)\right) \tag{2.5}$$

$$T_{p_t} = \frac{2}{3}\frac{R*\boldsymbol{k_r}*\boldsymbol{C_{r_r}}*r_3}{\boldsymbol{C_r}*r_1*pr}\frac{\left(T_2(y_j,t)-T_p(y_j,t)\right)}{Re} \tag{2.6}$$

Thus, the reduced system of ordinary differential equations in time, that is, for *i=1, 2, 3…, N*, and the system is solved by the above-mentioned four-stage order three *SSP RK43* scheme. At each stage of the scheme, the initial and boundary conditions *(19-20)* are considered accordingly. Hence the fluid velocity, temperature profiles v_1, T_1 of pure fluid in the region-I and fluid, particle velocity, and temperature profiles v_2, v_P, T_2, $T_P$of dusty fluid in the region-II have been numerically obtained in the fourth stage of MCB-DQM.

3. A-3. Numerical solution of immiscible dusty and pure fluids flow under the scheme-III.

To get the averaged flow velocity, reconstructed interface, and dust and particle velocity profiles under the scheme-III, replace the approximation of the spatial components of the first and second-order obtained by using MCB-DQM. Hence the system of single momentum coupled partial differential equations *(41-43)* followed by scheme III are updated as equations *(3.1-3.3)* then solved numerically, and the fluid and particle velocities profiles are obtained.

As ($-1 \le y \le 1$):

$$\frac{\partial C_i}{\partial t} = -v^*(y_j,t)\left(\sum_{j=1}^{N} a^*{}_{ij}C_i(y_j,t)\right) \tag{3.1}$$

$$\frac{\partial v^*}{\partial t} = \frac{Ge(t)}{1+C_s(r_2-1)} + \frac{(1+C_s(r_1-1))}{Re(\,1+C_s(r_2-1)\,)}\left(\sum_{j=1}^{N} b^*{}_{ij}v^*(y_j,t)\right) - \frac{R\,(1+C_s(r_1-1))}{Re(\,1+C_s(r_2-1)\,)}\Big(v^*(y_j,t) -$$

$$v_P(y_j,t)\Big) + \frac{1}{Fr} - \frac{1+C_s(r_1-1)}{Re*Ca(\,1+C_s(r_2-1)\,)}\left(\sum_{j=1}^{N} b^*{}_{ij}C_i(y_j,t)\,\right) \tag{3.2}$$

$$\frac{\partial v_P}{\partial t} = \frac{Rr_4\,(1+C_s(r_1-1))}{Re(1+r_2)}\Big(v^*(y_j,t) - v_P(y_j,t)\Big) \tag{3.3}$$

Thus, the reduced system of ordinary differential equations in time, that is, for i=1, 2, 3…, N, and the system is solved as above by a *four-stage order-three* SSP RK43 scheme. At each stage of the

scheme, the initial and boundary conditions *(39-40)* are considered accordingly. Hence the averaged flow, particle velocity profiles v^*, v_P and interface profile C_i have been obtained in the fourth stage of MCB-DQM.